

561283 58pgs

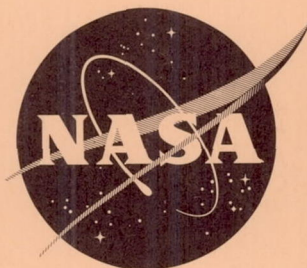
NASA TN D-1793

NASA TN D-1793

56p.

N 63 17301

Code-1



TECHNICAL NOTE

D-1793

CENTER-LINE PRESSURE DISTRIBUTIONS ON TWO-DIMENSIONAL
BODIES WITH LEADING-EDGE ANGLES GREATER THAN THAT
FOR SHOCK DETACHMENT AT MACH NUMBER 6 AND
ANGLES OF ATTACK UP TO 25°

By Theodore J. Goldberg, George C. Ashby, Jr.,
and James G. Hondros

Langley Research Center
Langley Station, Hampton, Va.

NATIONAL AERONAUTICS AND SPACE ADMINISTRATION
WASHINGTON

June 1963

TECHNICAL NOTE D-1793

CENTER-LINE PRESSURE DISTRIBUTIONS ON TWO-DIMENSIONAL
BODIES WITH LEADING-EDGE ANGLES GREATER THAN THAT
FOR SHOCK DETACHMENT AT MACH NUMBER 6 AND
ANGLES OF ATTACK UP TO 25° By Theodore J. Goldberg, George C. Ashby, Jr.,
and James G. Hondros

SUMMARY

17301

Center-line pressure distributions were obtained for two-dimensional sharp-nose parabolic arc, circular arc, and wedge bodies having a leading-edge angle greater than that for shock detachment (aerodynamically blunt bodies) at Mach number of 6 for angles of attack up to 25° . The maximum pressure coefficient was found to increase continuously from the shock-attachment value to the stagnation value behind a normal shock between leading-edge deflection angles of 42° and 51° . Only the data for contoured bodies having leading-edge angles of 66° or greater are correlated very well by the generalized Newtonian theory. However, at all angles of attack for all aerodynamically blunt bodies having curved surfaces, the agreement between the generalized Newtonian theory and the measured values of pressure coefficient was reasonably good for surface-deflection angles above 30° . This theory can be used to predict pressures on most two-dimensional bodies by the methods shown herein. With few exceptions, at a given deflection angle the pressure distributions rearward of the maximum pressure on the lower and upper surfaces of aerodynamically blunt wedges are essentially coincident with those of wedges having higher and lower half-angles, respectively. In addition, the pressure distributions of these wedges are in good agreement aft of the maximum-pressure point with those of a flat plate at corresponding deflection angles to the lower surface above 53° and to the upper surface above 31° .

INTRODUCTION

There is a large amount of available experimental and theoretical information in the hypersonic speed range for bodies having either rounded leading edges and therefore detached shock waves or sharp leading edges with attached shock waves. However there is very little, if any, available data in this speed range for the class of bodies with sharp leading edges having detached shock waves. The purpose of the present investigation is to provide some information in that area.

This report presents the center-line pressure distributions on a series of two-dimensional bodies having leading-edge angles from 42° to 90° which were measured in the Langley 20-inch Mach 6 tunnel at angles of attack up to 25° . In addition the means by which the pressure distributions can be predicted are also presented.

SYMBOLS

C_p	pressure coefficient, $\frac{p_1 - p_\infty}{\frac{1}{2}(\gamma p_\infty M_\infty^2)}$
M_∞	free-stream Mach number
p_1	local pressure, lb/sq in.
p_t	total or stagnation pressure, lb/sq in.
p_∞	free-stream pressure, lb/sq in.
s	distance along body surface from nose, in.
s_w	total length of wedge surface, in.
t	half the maximum body thickness, in.
x, y	body coordinates
α	angle of attack, deg
γ	ratio of specific heats
δ	local inclination of the body surface referenced to wind axis, deg
θ	local inclination of body surface referenced to body axis, deg
Subscripts:	
geom	geometric
l	lower surface
le	leading edge
max	maximum
stag	stagnation behind a normal shock
u	upper surface

APPARATUS AND METHODS

Wind Tunnel and Models

This investigation was conducted in the Langley 20-inch Mach 6 tunnel. The tunnel, which has been described in reference 1, is a blowdown-to-atmosphere type which operates at a maximum stagnation temperature of 600° F and a maximum stagnation pressure of 600 lb/sq in. The air is dried by an activated alumina dryer designed to provide a dewpoint temperature of -40° F at 600 lb/sq in.

The three groups of 5 two-dimensional models used in this investigation consisted of wedges and parabolic and circular arcs. Each group had leading-edge angles of 42°, 54°, 66°, 78°, and 90°. These models will herein be referred to by their leading-edge angles and contours. These contours were selected because they represent a large portion of the entire class of two-dimensional sharp-nose bodies having a leading-edge angle greater than that for shock detachment at a Mach number of 6. For a given deflection angle the wedge and the parabolic arc represent the minimum and maximum surface curvature of the present investigation, respectively, while the circular arc represents an intermediate curvature. Although the theoretical shock-detachment angle at Mach 6.0 is 42.4°, it was felt that a perfectly sharp leading edge could not be fabricated and that the shock for a 42°-leading-edge-angle model would be detached. This leading-edge angle would represent the lower limit of the aerodynamically blunt range. All models had a span of 4.00 inches and a thickness of 4.00 inches. The models were adapted with a 2.56-inch-long cylindrical section on the rear by using a "quick-disconnect" type connection to facilitate model changes. Photographs of the models and of the model attached to the support connection are shown in figures 1 and 2, respectively. Model dimensions are given in table I along with x,y locations of orifices, local inclinations at orifices, and surface distance-to-thickness ratios. Extensions, which were added to both sides of the 78° parabolic arc body to check the two dimensionality of the flow along the center line, were each 3 inches wide and contoured to match the basic body. A row of orifices on one of the extensions was located at the same position relative to the edge (2 inches inboard) as those on the basic body. This body was selected because it was the longest and any disturbance emanating from the tips of the models would affect the most rearward orifices. The 78° parabola with extensions is shown in figure 2. Model orifice sizes for the basic models and extensions were 0.021 inside diameter near the leading edges and 0.063 inside diameter at all other orifice locations.

The models were supported in the tunnel by the goose-neck support system shown in figure 3, which moved the model 25° in angle of attack in the horizontal plane. A mechanically operated counter geared to the vertical shaft of the support system was used to measure the angle of attack. Deflections due to air loads were negligible because of the stiffness of the sting support.

Tests

All models were tested in 5° increments over an angle-of-attack range of 0° to 25°. In addition, the 42°-leading-edge models were tested in 1° increments at angles of attack from 0° to 15°.

All tests reported herein were conducted at a stagnation pressure and temperature of 400 lb/sq in. absolute and 400° F which yields a Reynolds number of 7.6×10^6 per foot.

Pressure data were recorded by photographing a mercury manometer for pressures greater than 1 lb/sq in. absolute. For pressures of 1 lb/sq in. absolute or less a butyl phthalate manometer was used to obtain greater accuracy because of the low specific gravity of the fluid. Tunnel stagnation pressures were measured with a 0 to 600 lb/sq in. Bourdon gage. All pressures were photographically recorded simultaneously.

Data Reduction and Accuracy

Previous tunnel calibrations have shown that at any instant the Mach number throughout the test section varies by only ± 0.02 . However, the Mach number level varies from 5.94 to 6.04 depending upon time - the time during each run, the time between runs, and the total time elapsed. This fact makes it extremely difficult, if not impossible, to obtain an exact calibration curve of Mach number against time. The data, therefore, were initially reduced at an average Mach number of 6. This procedure resulted in sufficient data scatter to make difficult an analysis of data trends. One obvious trend emerged, however, which led to a better definition of test Mach numbers. This trend is shown in figure 4 where the maximum pressure coefficients obtained on the various bodies are presented as a function of the flow-deflection angles at which they were obtained. At flow-deflection angle for shock detachment ($\delta = 42^\circ$) the data agree with oblique shock theory. At higher flow-deflection angles the data approach and even exceed the stagnation-pressure-coefficient value at flow-deflection angles considerably less than 90° . The degree by which the data exceed $C_{p,stag}$, of course, is indicative of the data scatter. Since the data exceed $C_{p,stag}$ by as much as 4 percent which is much greater than measuring accuracy, the scatter is attributed to a true Mach number variation different from the assumed constant value of 6.0. By using the data trend shown in figure 4, a more representative Mach number variation for reducing the data was obtained by the following procedure. For each model the ratio of maximum-local to tunnel-stagnation pressure was assumed to be equal to the total pressure ratio across a normal shock. This ratio was then used to compute the corresponding Mach number for each model and α combination. At the angles of attack where the resulting Mach numbers fell within the known tunnel range these values of Mach number were used to reduce the data. The Mach numbers so obtained were applicable to all bodies except the 42° wedge at angles of attack below 7° and the 42° parabolic and circular arc bodies below $\alpha = 10^\circ$. For the 42° bodies at 0° angle of attack, the Mach numbers were computed by assuming the measured maximum pressure to be given by oblique shock theory. Since these Mach numbers again fell within the known range of tunnel Mach number, they were used to reduce the data for these models. For the angles of attack of the 42° bodies between 0° and 7° or 10° , as the case may be, a linear variation of Mach number with angle of attack between these limits was assumed. This assumption appears to be justifiable because the variation of tunnel Mach number with time is quasi-linear and in the same direction.

The center line of the body was considered to be the dividing line between the upper and lower surfaces at all angles of attack. The location of the maximum pressure point was determined from faired curves of P_1/P_t against θ on the upper and lower surfaces. Where no peak occurred beyond the first orifice, the values of P_1/P_t and θ at the first orifice were used to compute $C_{p,max}$ and δ_{max} . Where a peak occurred downstream of the first orifice, the faired values were used to compute $C_{p,max}$ and δ_{max} .

It should be noted that the data for the 78° parabolic arc body is the least reliable at angles of attack below 15° because the first orifice on the lower surface was inadvertently plugged. At 0° angle of attack the first orifice on the upper surface was used but it was located at an angle of about 8° less than that of the leading edge. At 5° and 10° angle of attack, the second orifice on the lower surface, which was located at an angle of about 12° less than the leading edge, was used. Therefore, the free-stream Mach number computed from the pressures at these orifices for these angles of attack is too high and results in a value of C_p which is too high. It is only this error in Mach number which raises a question as to the reliability of the data for the 78° body.

The maximum error of the measured pressures is believed to be less than 1 percent of the maximum measured value on the body. Model alignment and angles of attack are believed to be accurate to about $\pm 1/2^\circ$. The accuracy of the x,y coordinates of the model orifices is ± 0.001 inch. The measured coordinates were used to compute the slopes for all orifices.

RESULTS AND DISCUSSION

Experimental Results

Basic data.- The pressure distributions of the 78° parabolic arc model with and without extension pieces at $\alpha = -10^\circ$, 0° , and 10° are presented in figure 5 to show the two dimensionality of the flow. Flow blockage prevented any measurements at higher angles of attack; therefore, the agreement between the distributions on the body with and without the extensions establishes only that the flow along the center line of this, the longest, body is two dimensional up to $\alpha = 10^\circ$. However, all other bodies have the same span but are shorter; therefore, the flow along their center line, with the possible exception of the wedges having higher leading-edge angles, should also be two dimensional up to $\alpha = 10^\circ$.

Pressure distributions of the 15 models tested are presented in figures 6, 7, and 8 for angles of attack up to 25° . In addition, schlieren photographs of all the bodies near 0° angle of attack are presented in figure 9 to show the variation of the shock shape with changes in leading-edge angle and body contour.

Maximum pressure coefficient.- One of the most important results of these tests is that stagnation pressure occurs on all of the bodies in this investigation having a leading-edge deflection angle greater than about 51° and that the maximum pressure coefficient for all bodies has its locus along a single representative curve. (See fig. 10.) The portion of the curve between

shock-detachment angle and 51° may be questionable because of the small uncertainty in the value of free-stream Mach number and the inability to locate the first orifice directly at the apex of the nose. However, if the maximum known tunnel Mach numbers were used to compute the pressure coefficients for this portion of the curve, it would shift the deflection angle at which stagnation occurs only about 2° to approximately 49° . In reference 2 stagnation pressure on a flat plate was measured at a deflection angle of 45° . The unrealistic maximum pressure coefficients that are predicted for bodies in this investigation by two modifications to the Newtonian theory are also shown in figure 10 for comparison.

On the upper surface, figure 11 shows that all measured values of $C_{p,max}$ do not lie along a single curve but vary with leading-edge angle and angle of attack. However, for each leading-edge angle the values of $C_{p,max}$ for all shapes tested generally fall along the same curve with the exception of the 78° and 90° bodies. As the leading-edge angle increases, the variation of $C_{p,max}$ with deflection angle approaches that predicted by modified Newtonian theory until at $\delta_{\lambda e} = 90^\circ$ the curved-surface bodies agree with this theory.

Location of maximum pressure coefficients.- The location of the maximum pressures would be expected to occur at the point where the slope relative to the flow is the greatest - herein referred to as the geometric location. A comparison of the geometric and measured slopes at which the maximum pressures occurred on both the lower and upper surfaces of the parabolic and circular arc bodies is shown in figure 12. It must be remembered that physical limitations prevented the installation of the first orifice exactly at the leading edge. Therefore, in comparing the measured with the geometric location of $C_{p,max}$, they will be considered to coincide whenever the measured values differ from the geometric by the same difference as that indicated at 0° angle of attack. On the lower surface (fig. 12(a)) only for the 90° circular arc body do the measured and geometric locations coincide over the angle-of-attack range investigated. For all other bodies the measured location of $C_{p,max}$ moves off the nose before its angle relative to the flow becomes 90° . This result is attributed to the pressure bleed-off around the sharp leading edge. For bodies having leading-edge angles up to and including 66° , the measured location of $C_{p,max}$ moves off the nose when its angle relative to the flow becomes approximately 67° . This is also true for the wedges, as can be seen in figures 8(b) to (f). However, the maximum difference between the geometric and measured location for any body through the angle-of-attack range of the tests is only about 8° . On the upper surface the location of the maximum pressure might be expected to remain at the nose over the angle-of-attack range of the test. Figure 12(b) shows this to be true only for the 78° and 90° bodies. For bodies having leading-edge angles below 78° the location of $C_{p,max}$ is seen to move off the nose at angles of attack less than 20° . This result can be attributed to leading-edge separation around the nose followed by flow reattachment as indicated in figures 6, 7, and 8.

Comparison of center-line pressure distributions on wedges and a flat plate at corresponding deflection angles.- Another important result which can be obtained from these tests is the effect of leading-edge angle on the pressure distributions over the wedge surfaces at a given inclination to the flow. The

lower- and upper-surface pressure distributions, in terms of $C_p/C_{p,max}$ against s/s_w for wedges at approximately constant surface-deflection angles are presented in figure 13. The surface-deflection angles are only approximately constant because the wedge angles were varied in 12° increments whereas the angle of attack was varied in 5° increments. It can be seen that the maximum pressure point moves rearward on the lower surface with decreasing wedge angle only for deflection angles greater than about 66° and on the upper surface with increasing wedge angle only for deflection angles less than about 66° . The effect of leading-edge angle on wedge surface-pressure distributions is seen to be slight because, with few exceptions, at a given deflection angle, the pressure distributions rearward of the maximum pressure point on the lower and upper surfaces are essentially coincident with those of corresponding surfaces of wedges having higher and lower half-angles, respectively. Thus the wedge-surface pressure distributions are primarily a function only of flow-deflection angles. The effect of leading edge is confined to those regions ahead of the location of the maximum pressure coefficient. Since the value of $C_{p,max}$ on the lower surface is a constant (as shown in fig. 13), the pressure coefficients aft of the maximum pressure point on the lower surface at a given location of all wedges at the same deflection angles are also coincident. However, on the upper surface the value of $C_{p,max}$ varies not only with deflection angle but also with wedge angle at the same deflection angle; therefore, the pressure coefficients at a given location on the upper surface of wedges at the same deflection angles are not coincident. It should be noted that at $\delta = 66^\circ$ and above, the distributions on the lower and upper surfaces for the same δ agree. This can be seen from figures 13(a) and 13(b) since the data for each body at $\alpha = 0$ are presented in both.

Also included in figure 13 are flat-plate pressure distributions from reference 2 at approximately the same deflection angles as the wedge surfaces. In general, the pressure distributions of the wedges are in good agreement aft of the maximum pressure point with those of the flat plate at deflection angles of the lower surface above 53° and of the upper surface above 31° . This agreement might not be envisioned since in a subsonic-flow field behind a normal shock, the upper surface would be expected to affect the pressures on the lower surface of the wedge. It is interesting to note that for deflection angles from 27° to 37° the values of $C_{p,max}$ for the upper surface of wedges at angles of attack other than 0° are about the same as those for a flat plate at corresponding deflection angles.

Prediction of Pressures on Aerodynamically Blunt Bodies

Having obtained the pressure data on these bodies it is of interest to determine if there is a simple method of predicting pressures on two-dimensional aerodynamically blunt bodies. Probably the most widely used method of predicting pressures and forces (because of its simplicity and ease of calculating) is some form of the Newtonian theory

$$C_p = K \sin^2 \delta$$

Various modifications of this theory have been found to give reasonably good predictions of the pressure distribution on different bodies, if the proper value of K is chosen. For example, it is shown in reference 3 that with $K = (\gamma + 1)$, the theory is applicable only to bodies having small leading-edge angles; and in reference 4, with $K = C_{p,stag}$, theory is limited to bodies having 90° leading-edge slopes. As can be seen in figure 10, neither of these modifications is applicable to the bodies of this investigation.

A more recent consideration of the Newtonian theory is presented in reference 5 which suggests that in the general case K has the form $\frac{C_{p,max}}{\sin^2 \delta_{max}}$, thus acknowledging that K is not necessarily constant. This resulted in the generalized Newtonian theory

$$\frac{C_p}{C_{p,max}} = \frac{\sin^2 \delta}{\sin^2 \delta_{max}}$$

which was shown to predict the surface-pressure distribution reasonably well for pointed-nose bodies having a leading-edge angle less than that for shock detachment, as well as for bodies having a 90° leading-edge slope. (Unpublished work also shows that this generalized form of Newtonian theory can be derived by resorting to the tangent-wedge or tangent-cone approximations.) Therefore, it was decided to investigate this method for use in predicting the pressures on the two-dimensional aerodynamically blunt bodies studied herein.

Wedges.- Since the prediction of the pressure distribution for any body by means of the generalized Newtonian theory is basically dependent upon the body having a changing slope, it obviously cannot be applied in the same manner to wedges as to bodies having curved surfaces. However, it is shown in reference 5, that by using pressures computed from attached shock theory, the generalized Newtonian theory is applicable from one wedge to another, for wedge angles less than shock detachment at 0° angle of attack. For the aerodynamically blunt wedges of the present investigation it is apparent from figure 8 that the large and varied pressure gradients require any correlation with generalized Newtonian theory from one wedge to another, or from one surface to another for the same wedge at angle of attack, to be made at more than one point along the surface of the bodies. Even if this could be done with reasonably good results, the pressure distribution of one wedge would first have to be known. In view of the fact that experimental values must be resorted to, and since the data of the present investigation cover the range of aerodynamically blunt wedges, the pressure distribution of any wedge in this regime can be obtained by interpolating these data. In addition, the good agreement in pressure distribution from wedge to wedge at the same deflection angles, as well as the agreement from wedges to a flat plate at corresponding deflection angles (fig. 13), enables the pressure distribution to be obtained for either of the two types of bodies if one is known.

Parabolic and circular arc bodies.- Since the lower and upper surfaces of the bodies of the present investigation are separated by a sharp leading edge, which is shown in figures 6 and 7 to result in flow separation and reattachment

at some angles of attack and, therefore, a difference in the value of K between the two surfaces, the theory might not be expected to apply from surface to surface. Therefore, the data for each surface are reduced in the generalized Newtonian form by using their respective measured $C_{p,max}$ values. The results for the parabolic and circular arc models together with the generalized Newtonian theory prediction using the measured $C_{p,max}$ and its associated δ_{max} are presented in figures 14 and 15.

As can be seen from figures 14 and 15, the data for both the parabolic arc and circular arc bodies can be divided into two distinct correlation groups; bodies having a leading-edge angle closest to that for shock attachment (42° and 54°) and bodies having leading-edge angles much greater than shock attachment (66° to 90°). The data for the former group are not correlated with any consistency by the generalized Newtonian theory, whereas the data of the latter group were in general correlated very well for both surfaces by the theory.

The agreement between the measured and theoretical values in percent of the measured C_p cannot be made directly from figures 14 and 15 because the $C_{p,max}$ values are not constant for all bodies on either surface. Therefore, a majority of the measured and predicted values of C_p together with their differences in percent of measured C_p are presented in table II. As might be expected the agreement is best near the nose where the body slope is high and becomes progressively poorer as the surface inclination decreases; however, the disagreement does not in general become poorer than about 20 percent of measured C_p down to a surface inclination of 30° (the limit to which modified Newtonian theory is known to predict the pressures very well on cylinders). The very high percentage errors at inclinations below 30° may not be very significant because the pressures are very low over this region. There are points between the nose and the maximum pressure point on both surfaces of some bodies at angle of attack which cannot be predicted by the generalized Newtonian theory because the value of $\frac{\sin^2 \delta}{\sin^2 \delta_{max}}$ becomes greater than 1. But considering all points above deflection angles of 30° , the theory predicts about 85 percent of them within 10 percent of the measured C_p . It should be noted that whereas the data for the lower surface appear to be in better agreement with the theory than those of the upper surface in figures 14 and 15, table II shows that, on the basis of the percentage of measured C_p , both surfaces show about the same agreement for inclinations above 30° . The agreement for the circular arc bodies was, in general, better than that for the parabolic arc bodies and indicated that for the same leading-edge angle the gradient of slope along the body may be the important factor in determining how well the generalized Newtonian theory predicts the pressure distribution for two-dimensional aerodynamically blunt bodies, that is, the more rapidly the slope changes, the poorer the correlation.

Application of Generalized Newtonian Theory to Any Two-Dimensional

Aerodynamically Blunt Body Having Curved Surfaces

It has been shown that the pressure distributions of the aerodynamically blunt bodies having curved surfaces of the present investigation agree reasonably well with the generalized Newtonian theory. However, in order to use this theory to predict the pressures on any body without resorting to experimentation, it is necessary to know a pressure at a given slope on the surface. Since the measured locations of the maximum pressures are shown in figure 12 to occur reasonably close to the geometric locations and because the maximum pressure on the lower surface is equal to stagnation value for the majority of deflection angles between shock detachment and 90° (fig. 10), it would be convenient to utilize the maximum pressure on the lower surface to predict the pressures over the whole body. An analysis shows that this can be accomplished as follows:

On the lower surface $C_{p,max} = C_{p,stag}$ for $\delta_{\lambda e} \geq 51^\circ$, while for $\delta < 51^\circ$, $C_{p,max}$ for deflection angles between 42° and 51° can be obtained from

$$\frac{C_{p,max}}{C_{p,stag}} = \frac{\sin^2 \delta_{\lambda e}}{\sin^2 51^\circ}$$

The values of $C_{p,max}$ obtained in this manner for these deflection angles are shown in figure 10 and are in good agreement with the measured values. For deflection angles equal to or less than shock detachment, $C_{p,max}$ is obtained from oblique shock theory.

The pressure distribution for the lower surface at each angle of attack can then be computed from

$$\frac{C_p}{C_{p,max}} = \frac{\sin^2 \delta}{\sin^2 \delta_{max,geom}}$$

and the pressure distributions for the upper surface can be obtained at any angle of attack from

$$\frac{C_p}{C_{p,max}(\alpha=0^\circ)} = \frac{\sin^2 \delta}{\sin^2 \delta_{\lambda e}(\alpha=0^\circ)}$$

The pressure coefficients predicted by this method for the parabolic and circular arc bodies are presented in table II. In general, these values are about the same as those obtained from the generalized Newtonian theory by using the values of $C_{p,max}$ at their actual locations on each surface and are within about 20 percent of the measured C_p at deflection angles above 30° . Some of the points between the nose and the actual location of the maximum pressure point, which could not be predicted by the generalized Newtonian theory by using $C_{p,max}$ at

its actual location for each surface, are not predicted by this method within this accuracy. However, on the whole, about 85 percent of all points at deflection angles above 30° are predicted within 10 percent of the measured C_p value.

The good agreement between the generalized Newtonian theory and the data of the present investigation as well as the results for bodies having a leading-edge angle less than that for shock detachment in reference 5 indicate that this theory may be applicable to all two-dimensional bodies except aerodynamically blunt wedges.

CONCLUSIONS

An investigation of the center-line pressure distributions on two-dimensional sharp-nose bodies having a leading-edge angle greater than that for shock detachment at a Mach number of 6 and angles of attack up to 25° has resulted in the following conclusions:

1. Stagnation pressure behind a normal shock was measured on all bodies having a leading-edge deflection angle greater than about 51° and the maximum pressure coefficient for all bodies has its locus along a single representative curve which continuously increases with increasing deflection angle between shock detachment and about 51° .

2. With few exceptions the center-line pressure distributions rearward of the maximum pressure point on the lower and upper surfaces of aerodynamically blunt wedges are primarily a function only of surface-deflection angle and essentially independent of leading-edge angle. In addition, the pressure distributions of these wedges are in good agreement aft of the maximum pressure point with those of a flat plate at corresponding deflection angles to the lower surface above 53° and to the upper surface above 31° .

3. Only the data for contoured bodies having leading-edge angles of 66° or greater are correlated very well by the generalized Newtonian theory. However, at all angles of attack for all aerodynamically blunt bodies having curved surfaces, the agreement between the generalized Newtonian theory and the measured values of C_p was reasonably good for surface-deflection angles above 30° (for 85 percent of the points in this region the theoretical values of C_p were within 10 percent of the measured C_p).

4. The generalized Newtonian theory can be used to predict the center-line pressures on aerodynamically blunt contoured bodies because the maximum pressures and their locations can be predetermined.

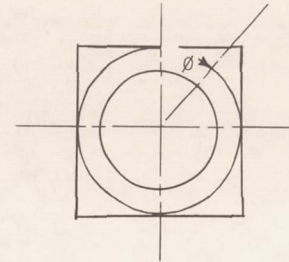
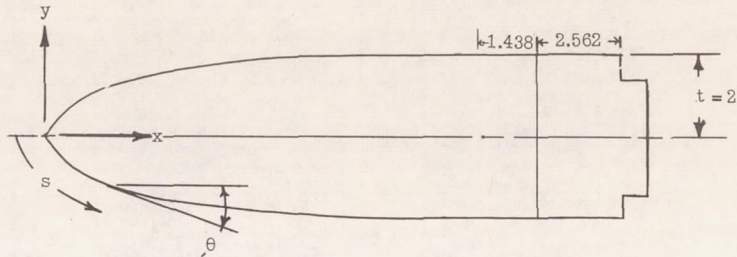
Langley Research Center,
National Aeronautics and Space Administration,
Langley Station, Hampton, Va., February 27, 1963.

REFERENCES

1. Ashby, George C., Jr., and Fitzgerald, Paul E., Jr.: Longitudinal Stability and Control Characteristics of Missile Configurations Having Several Highly Swept Cruciform Fins and a Number of Trailing-Edge and Fin-Tip Controls at Mach Numbers From 2.21 to 6.01. NASA TM X-335, 1961.
2. Hondros, James G.: Pressure Distributions on Two-Dimensional Sharp-Leading-Edge Flat Plates With Sweep Angles of 0° , 30° , and 45° at a Mach Number of 6 and Angles of Attack From 0° to 90° . NASA TN D-1371, 1962.
3. Laitone, Edmund V.: Exact and Approximate Solutions of Two-Dimensional Oblique Shock Flow. Jour. Aero. Sci., vol. 14, no. 1, Jan. 1947, pp 25-41.
4. Lees, Lester: Hypersonic Flow. Fifth International Aeronautical Conference (Los Angeles, Calif., June 20-23, 1955), Inst. Aero. Sci., Inc., 1955, pp 241-276.
5. Love, E. S.: Generalized-Newtonian Theory. Jour. Aero/Space Sci. (Reader's Forum), vol. 26, no. 5, May 1959, pp. 314-315.

TABLE I.- MODEL DIMENSIONS AND ORIFICE LOCATIONS

(a) Parabolic arc models



42° parabolic arc					
Orifice location		Slope θ, deg	s/t	φ, deg	
x, in.	y, in.				
0.067	-0.060	41.23	0.045	180	
.226	-.196	39.44	.149		
.407	-.342	37.46	.265		
.565	-.457	35.80	.363		
.726	-.568	34.15	.441		
1.227	-.880	29.33	.756		
1.512	-1.033	26.80	.918		
1.861	-1.199	23.88	1.110		
2.255	-1.358	20.82	1.324		
2.698	-1.512	17.66	1.558		
3.829	-1.792	10.75	2.142		
4.306	-1.873	8.26	2.383		
4.774	-1.933	6.02	2.619		
5.241	-1.975	3.97	2.854		
5.720	-1.999	2.03	3.093		
6.999	-2.000	0	3.733		
.172	.148	40.01	.114		0
.282	.236	38.82	.185		
.412	.338	37.41	.268		
.571	.456	35.73	.367		
.730	.569	34.11	.464		
.968	.725	31.76	.606		
1.226	.877	29.44	.755		
1.518	1.034	26.90	.921		
1.862	1.197	23.87	1.111		
2.257	1.359	20.81	1.325		
2.702	1.512	17.64	1.560		
3.836	1.794	10.71	2.113		
4.305	1.871	8.26	2.383		
4.776	1.932	6.01	2.620		
5.242	1.972	3.97	2.854		
5.718	1.994	2.05	3.092		
6.174	2.000	.35	3.321		
6.431	2.000	0	3.449		

54° parabolic arc					
Orifice location		Slope θ, deg	s/t	φ, deg	
x, in.	y, in.				
0.036	-0.052	53.04	0.030	180	
.140	-.180	50.39	.114		
.275	-.332	47.19	.217		
.415	-.476	44.12	.317		
.610	-.654	40.21	.448		
.792	-.799	36.92	.565		
1.106	-1.065	31.89	.755		
1.446	-1.206	27.22	.951		
1.875	-1.403	22.27	1.187		
2.422	-1.601	17.10	1.477		
3.497	-1.850	9.54	2.029		
3.972	-1.923	6.96	2.269		
4.564	-1.975	4.21	2.567		
5.097	-1.996	2.09	2.834		
5.427	-1.997	.90	2.999		
6.701	-1.998	0	3.636		
.122	.156	50.83	.100		0
.194	.242	49.08	.156		
.275	.332	47.19	.217		
.419	.481	44.03	.320		
.610	.655	40.21	.448		
.793	.802	36.90	.565		
1.100	1.062	31.97	.752		
1.451	1.212	27.17	.953		
1.872	1.405	22.30	1.185		
2.423	1.602	17.10	1.478		
3.502	1.852	9.51	2.032		
4.030	1.924	6.37	2.298		
4.566	1.973	4.21	2.569		
5.097	1.988	2.09	2.834		
5.432	1.999	.89	3.002		
5.909	1.999	0	3.240		

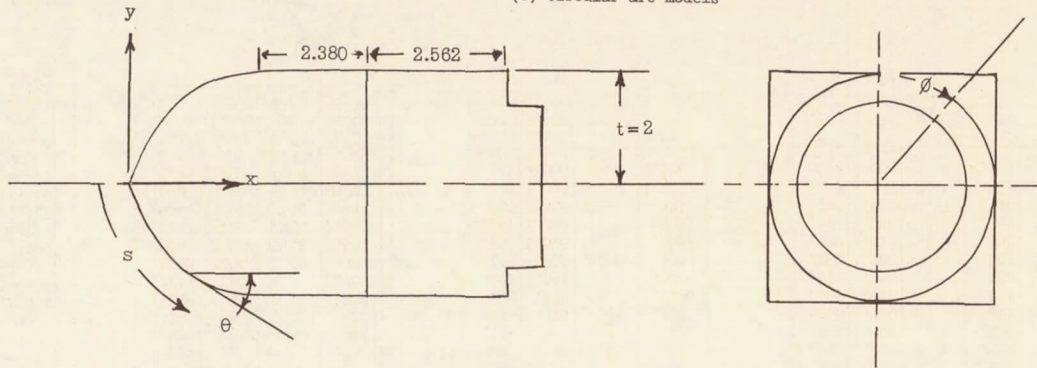
66° parabolic arc					
Orifice location		Slope θ, deg	s/t	φ, deg	
x, in.	y, in.				
0.026	-0.068	64.19	0.031	180	
.105	-.202	59.35	.114		
.195	-.335	54.70	.197		
.293	-.468	50.37	.278		
.402	-.592	46.23	.360		
.664	-.829	38.33	.536		
.985	-1.051	31.22	.732		
1.446	-1.291	23.96	.992		
2.155	-1.521	16.54	1.369		
3.049	-1.761	10.53	1.829		
3.569	-1.846	7.99	2.092		
4.092	-1.910	5.90	2.355		
4.612	-1.958	4.16	2.616		
5.128	-1.987	2.69	2.875		
5.655	-1.998	1.38	3.138		
6.182	-2.000	.25	3.402		
7.265	-2.000	0	3.950		
.073	.147	61.21	.082		0
.134	.251	57.75	.142		
.196	.341	54.65	.198		
.299	.475	50.12	.282		
.406	.595	46.09	.362		
.667	.832	38.25	.538		
.988	1.053	31.17	.733		
1.448	1.291	23.94	.993		
2.055	1.518	17.41	1.317		
3.059	1.764	10.48	1.833		
3.567	1.846	8.00	2.091		
4.095	1.911	5.89	2.337		
4.617	1.958	4.15	2.619		
5.138	1.989	2.66	2.871		
5.653	1.999	1.39	3.138		
6.193	1.999	.22	3.407		
6.461	1.999	0	3.541		

78° parabolic arc				
Orifice location		Slope θ, deg	s/t	φ, deg
x, in.	y, in.			
0.015	-0.069	73.93	0.031	180
.052	-.164	66.82	.086	
.108	-.267	59.51	.148	
.166	-.367	53.79	.215	
.235	-.462	48.87	.287	
.309	-.551	44.62	.361	
.391	-.634	40.96	.437	
.478	-.711	37.83	.515	
.570	-.782	35.19	.595	
.666	-.848	33.01	.677	
.766	-.909	31.17	.761	
.870	-.965	29.64	.847	
.978	-1.016	28.38	.935	
1.090	-1.062	27.34	1.025	
1.206	-1.104	26.47	1.117	
1.326	-1.141	25.74	1.211	
1.450	-1.174	25.12	1.307	
1.578	-1.202	24.58	1.405	
1.710	-1.226	24.11	1.505	
.025	.084	70.56	.048	
.062	.183	65.35	.098	
.102	.260	60.19	.142	
.146	.328	56.06	.190	
.194	.381	52.82	.239	
.246	.430	50.44	.291	
.302	.475	48.87	.345	
.362	.518	47.96	.400	
.426	.559	47.59	.457	
.494	.598	47.67	.515	
.566	.635	48.17	.574	
.642	.669	48.99	.634	
.722	.700	49.99	.694	
.804	.729	51.11	.755	
.888	.756	52.31	.817	
.974	.780	53.56	.880	
1.062	.801	54.91	.944	
1.152	.819	56.32	1.009	
1.244	.834	57.77	1.075	

90° parabolic arc				
Orifice location		Slope θ, deg	s/t	φ, deg
x, in.	y, in.			
0.000	-0.007	89.62	0.004	180
.005	-.117	83.50	.051	
.019	-.214	77.79	.099	
.055	-.333	70.43	.167	
.124	-.480	61.21	.252	
.245	-.655	49.48	.333	
.416	-.855	35.22	.436	
.646	-1.076	20.64	.564	
.934	-1.321	10.16	.719	
1.280	-1.586	4.21	.899	
1.694	-1.867	0	1.099	
2.176	-2.160	0	1.319	
2.726	-2.464	0	1.559	
3.344	-2.776	0	1.819	
4.030	-3.094	0	2.099	
4.784	-3.426	0	2.399	
5.606	-3.772	0	2.719	
6.496	-4.132	0	3.059	
7.454	-4.506	0	3.419	
8.480	-4.896	0	3.799	

TABLE I.- MODEL DIMENSIONS AND ORIFICE LOCATIONS - Continued

(b) Circular arc models



42° circular arc					
Orifice location		Slope θ , deg	s/t	ϕ , deg	
x, in.	y, in.				
0.082	-0.075	41.19	0.056	180	
.203	-.179	40.01	.136	0	
.278	-.239	39.30	.183		
.481	-.399	37.41	.312		
.675	-.542	35.63	.432		
.979	-.751	32.91	.618		
1.226	-.906	30.77	.764		
1.488	-1.053	28.56	.913		
1.979	-1.298	24.51	1.188		
2.27	-1.423	22.19	1.345		
3.036	-1.690	16.21	1.752		
3.567	-1.823	12.18	2.022		
4.082	-1.918	8.33	2.289		
4.609	-1.980	4.42	2.575		
5.121	-1.997	.66	2.749		
6.212	-1.998	0	3.293		
.162	.139	40.43	.105		0
.287	.243	39.24	.187		
.363	.305	38.51	.236		
.592	.480	36.39	.380		
.747	.592	34.99	.476		
.979	.749	32.92	.616		
1.233	.910	30.71	.768		
1.583	1.104	27.76	.967		
1.979	1.298	24.51	1.188		
2.273	1.424	22.16	1.347		
3.037	1.690	16.20	1.751		
3.567	1.823	12.18	2.022		
4.083	1.919	8.32	2.292		
4.609	1.982	4.42	2.586		
5.127	1.997	.62	2.738		
5.410	1.999	0	2.879		

54° circular arc					
Orifice location		Slope θ , deg	s/t	ϕ , deg	
x, in.	y, in.				
0.046	0.064	53.07	0.040	180	
.117	-.154	51.71	.097	0	
.195	-.247	50.29	.156		
.302	-.370	48.36	.237		
.422	-.500	46.27	.326		
.538	-.619	44.31	.409		
.721	-.789	41.36	.535		
.941	-.973	37.96	.679		
1.149	-1.127	34.91	.808		
1.376	-1.275	31.71	.943		
1.592	-1.399	28.77	1.067		
2.430	-1.762	17.96	1.524		
2.905	-1.890	12.15	1.769		
3.375	-1.967	6.52	2.002		
3.843	-1.995	.97	2.177		
4.932	-1.998	0	2.722		
.081	.105	52.44	.066		0
.183	.231	50.53	.146		
.285	.351	48.66	.225		
.342	.415	47.65	.268		
.472	.554	45.40	.364		
.605	.685	43.19	.457		
.736	.803	41.11	.545		
.919	.955	38.30	.664		
1.121	1.107	35.32	.791		
1.362	1.317	31.59	.984		
1.591	1.402	28.76	1.069		
2.434	1.765	17.91	1.529		
2.905	1.892	12.14	1.773		
3.377	1.968	6.49	2.005		
3.849	1.999	.90	2.226		
4.125	1.999	0	2.363		

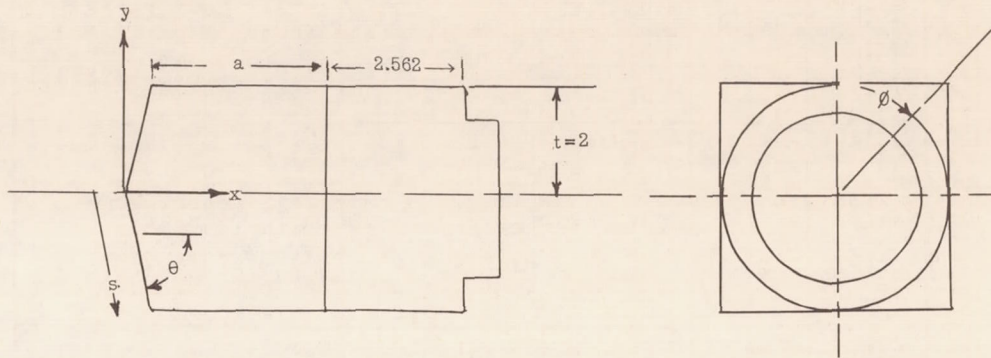
66° circular arc					
Orifice location		Slope θ , deg	s/t	ϕ , deg	
x, in.	y, in.				
0.016	-0.039	65.28	0.021	180	
.060	-.128	63.59	.070	0	
.111	-.225	61.74	.125		
.177	-.341	59.45	.192		
.253	-.465	56.98	.265		
.382	-.647	53.19	.376		
.495	-.794	50.05	.469		
.611	-.922	47.10	.555		
.763	-1.079	43.39	.665		
.906	-1.207	40.12	.761		
1.111	-1.366	35.71	.891		
1.342	-1.517	31.04	1.028		
2.027	-1.834	18.18	1.411		
2.506	-1.952	9.79	1.656		
3.018	-1.997	1.04	1.876		
4.094	-2.000	0	2.414		
.058	.126	63.64	.070		0
.116	.238	61.49	.133		
.159	.314	60.01	.176		
.245	.455	57.37	.259		
.340	.595	54.33	.343		
.436	.722	51.63	.423		
.533	.839	49.04	.499		
.643	.958	46.29	.579		
.761	1.076	43.45	.663		
.906	1.208	40.12	.762		
1.108	1.366	35.76	.891		
1.325	1.510	31.33	1.022		
2.016	1.830	18.37	1.404		
2.497	1.950	9.94	1.652		
3.004	1.998	1.29	1.891		
3.361	2.000	0	2.069		

78° circular arc					
Orifice location		Slope θ , deg	s/t	ϕ , deg	
x, in.	y, in.				
0.004	-0.042	77.04	0.023	180	
.022	-.128	75.05	.068	0	
.047	-.214	73.02	.112		
.089	-.329	70.27	.173		
.149	-.474	66.70	.251		
.208	-.599	63.57	.319		
.274	-.722	60.39	.389		
.382	-.899	55.70	.493		
.493	-1.051	51.43	.588		
.597	-1.171	47.83	.667		
.750	-1.325	42.90	.776		
.967	-1.506	36.49	.917		
1.174	-1.644	30.85	1.042		
2.072	-1.968	9.06	1.521		
2.386	-1.997	1.89	1.665		
3.470	-1.999	0	2.207		
.028	.124	75.11	.066		0
.056	.218	72.89	.114		
.091	.319	70.46	.167		
.147	.456	67.10	.241		
.205	.584	63.91	.311		
.273	.714	60.56	.385		
.351	.845	57.11	.461		
.445	.981	53.34	.544		
.544	1.105	49.76	.623		
.643	1.216	46.37	.698		
.744	1.315	43.16	.768		
.950	1.490	37.03	.904		
1.152	1.628	31.47	1.026		
2.039	1.964	9.82	1.507		
2.373	1.997	2.19	1.659		
2.678	1.999	0	1.811		

90° circular arc					
Orifice location		Slope θ , deg	s/t	ϕ , deg	
x, in.	y, in.				
0.001	-0.003	89.91	0.001	180	
.002	-.073	87.90	.036	0	
.011	-.190	84.53	.095		
.028	-.323	80.71	.162		
.056	-.461	76.64	.232		
.089	-.582	73.06	.295		
.134	-.714	69.05	.365		
.215	-.897	63.31	.465		
.279	-1.014	59.47	.532		
.373	-1.156	54.59	.616		
.503	-1.322	48.54	.722		
.611	-1.538	44.00	.802		
.822	-1.614	36.11	.939		
1.523	-1.940	13.80	1.326		
1.929	-1.996	2.04	1.507		
3.004	-2.000	0	2.045		
.004	.089	87.45	.044		0
.009	.170	85.13	.085		
.021	.275	82.07	.138		
.042	.390	78.73	.196		
.071	.518	74.97	.261		
.112	.648	71.05	.330		
.176	.813	65.96	.418		
.239	.941	61.88	.489		
.318	1.076	57.39	.568		
.397	1.190	53.40	.637		
.505	1.322	48.51	.722		
.618	1.459	43.82	.803		
.826	1.614	36.02	.939		
1.508	1.934	14.27	1.314		
1.924	1.995	2.17	1.503		
2.204	1.999	0	1.643		

TABLE I. - MODEL DIMENSIONS AND ORIFICE LOCATIONS - Concluded

(c) Wedge models



42° wedge					
Orifice location		Slope θ , deg	s/t	ϕ , deg	
x, in.	y, in.				
0.054	-0.048	42.00	0.036	180	
.203	-.185				
.357	-.321				
.459	-.413				
.573	-.516				
.761	-.684				
.944	-.850				
1.125	-1.012				
1.320	-1.188				
1.498	-1.349				
1.687	-1.518				
2.145	-1.931				
3.216	-2.000				
.149	.134		42.00		0
.256	.230		0		0
.364	.328				
.476	.428				
.575	.517				
.765	.689				
.949	.855				
1.141	1.027				
1.326	1.192				
1.510	1.358				
1.691	1.523				
2.155	1.941				
2.417	2.000				

a = 1.438

54° wedge					
Orifice location		Slope θ , deg	s/t	ϕ , deg	
x, in.	y, in.				
0.046	-0.063	54.00	0.039	180	
.132	-.181				
.231	-.318				
.318	-.438				
.410	-.565				
.560	-.771				
.704	-.970				
.934	-1.285				
1.037	-1.428				
1.146	-1.579				
1.406	-1.936				
2.448	-2.000				
.099	.137		0		0
.164	.226				
.231	.318				
.324	.446				
.417	.574				
.564	.777				
.714	.982				
.932	1.284				
1.042	1.435				
1.148	1.581				
1.412	1.944				
1.548	2.000				

a = 2.063

66° wedge					
Orifice location		Slope θ , deg	s/t	ϕ , deg	
x, in.	y, in.				
0.025	-0.057	66.00	0.031	180	
.077	-.172				
.138	-.309				
.198	-.445				
.255	-.574				
.359	-.806				
.453	-1.017				
.547	-1.229				
.634	-1.424				
.844	-1.895				
1.876	-2.000				
.046	.102		0		0
.094	.210				
.136	.304				
.190	.428				
.266	.597				
.355	.796				
.452	1.016				
.547	1.228				
.630	1.415				
.837	1.878				
1.101	2.000				

a = 2.625

78° wedge					
Orifice location		Slope θ , deg	s/t	ϕ , deg	
x, in.	y, in.				
0.002	-0.011	78.00	0.005	180	
.028	-.133				
.061	-.288				
.087	-.411				
.117	-.548				
.168	-.788				
.219	-1.030				
.274	-1.288				
.325	-1.531				
.404	-1.898				
1.422	-2.000				
.022	.102		0		0
.044	.208				
.068	.320				
.089	.418				
.117	.552				
.168	.788				
.222	1.041				
.274	1.290				
.297	1.400				
.408	1.921				
.622	2.000				

a = 3.090

90° wedge					
Orifice location		Slope θ , deg	s/t	ϕ , deg	
x, in.	y, in.				
0.000	0.000	90.00	0.000	180	
.109	-.109				
.199	-.199				
.314	-.314				
.449	-.449				
.696	-.696				
.945	-.945				
1.096	-1.096				
1.246	-1.246				
1.394	-1.394				
1.915	-1.915				
.995	.000		0		0
.112	.112				
.200	.200				
.333	.333				
.455	.455				
.700	.700				
.958	.958				
1.079	1.079				
1.206	1.206				
1.335	1.335				
1.930	1.930				
.198	2.000				

a = 3.515

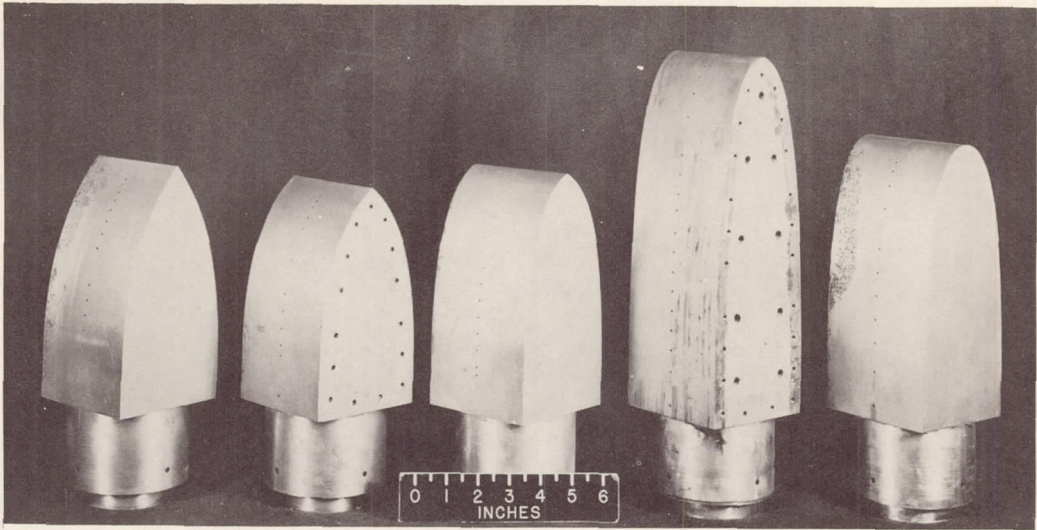
TABLE II.- MEASURED AND THEORETICAL VALUES OF PRESSURE COEFFICIENTS FOR

TWO-DIMENSIONAL AERODYNAMICALLY BLUNT BODIES - Continued

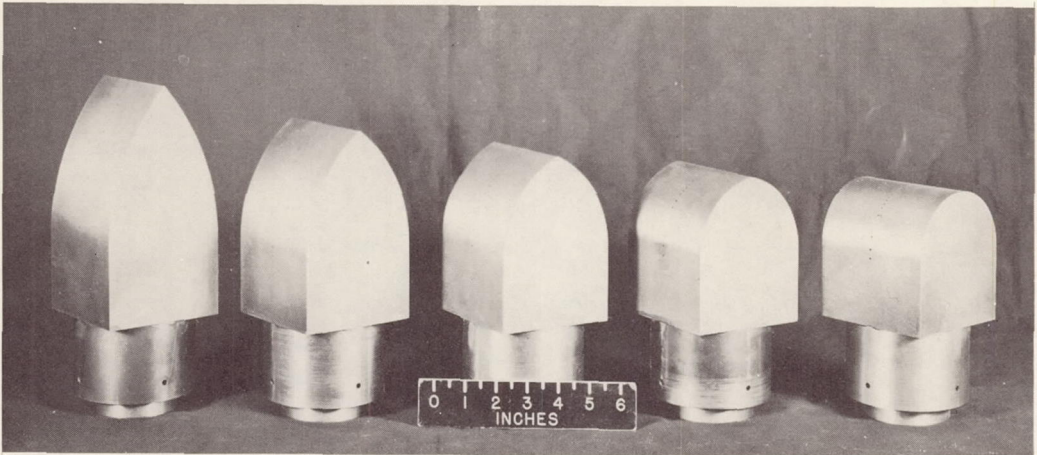
(c) Circular arc bodies - lower surface

$\theta_{le} = 42^\circ$										$\theta_{le} = 54^\circ$										$\theta_{le} = 66^\circ$																					
α , deg	δ , deg	$C_{p,meas}$	C_p	C_p	$C_{p,meas} - C_p$		α , deg	δ , deg	$C_{p,meas}$	C_p	C_p	$C_{p,meas} - C_p$		α , deg	δ , deg	$C_{p,meas}$	C_p	C_p	$C_{p,meas} - C_p$		α , deg	δ , deg	$C_{p,meas}$	C_p	C_p	$C_{p,meas} - C_p$															
					$C_{p,meas}$	C_p						$C_{p,meas}$	C_p						$C_{p,meas}$	C_p						$C_{p,meas}$	C_p	$C_{p,meas}$	C_p												
0	41.19	1.2802	1.2798	1.2397	0.00031	0.03164	0	53.07	1.8182	1.8181	1.7749	0.00005	0.02381	0	65.28	1.8182	1.8184	1.7977	-0.00011	0.01127	0	41.19	1.2802	1.2798	1.2397	0.00031	0.03164	0	53.07	1.8182	1.8181	1.7749	0.00005	0.02381	0	65.28	1.8182	1.8184	1.7977	-0.00011	0.01127

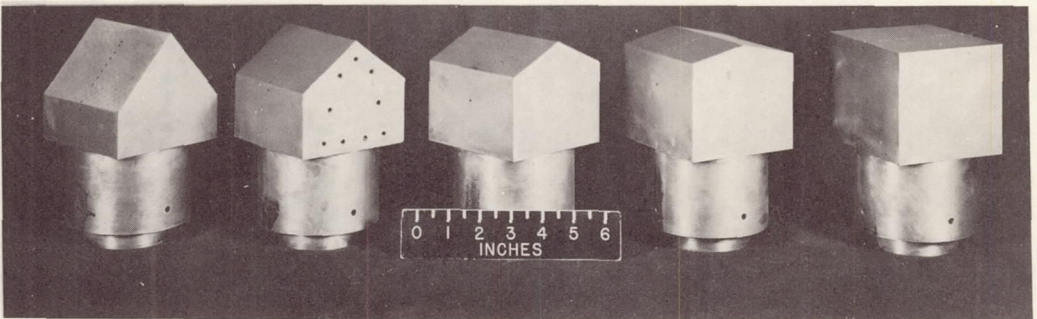
^{a,b}See footnotes at end of table.



(a) Parabolic arc models.



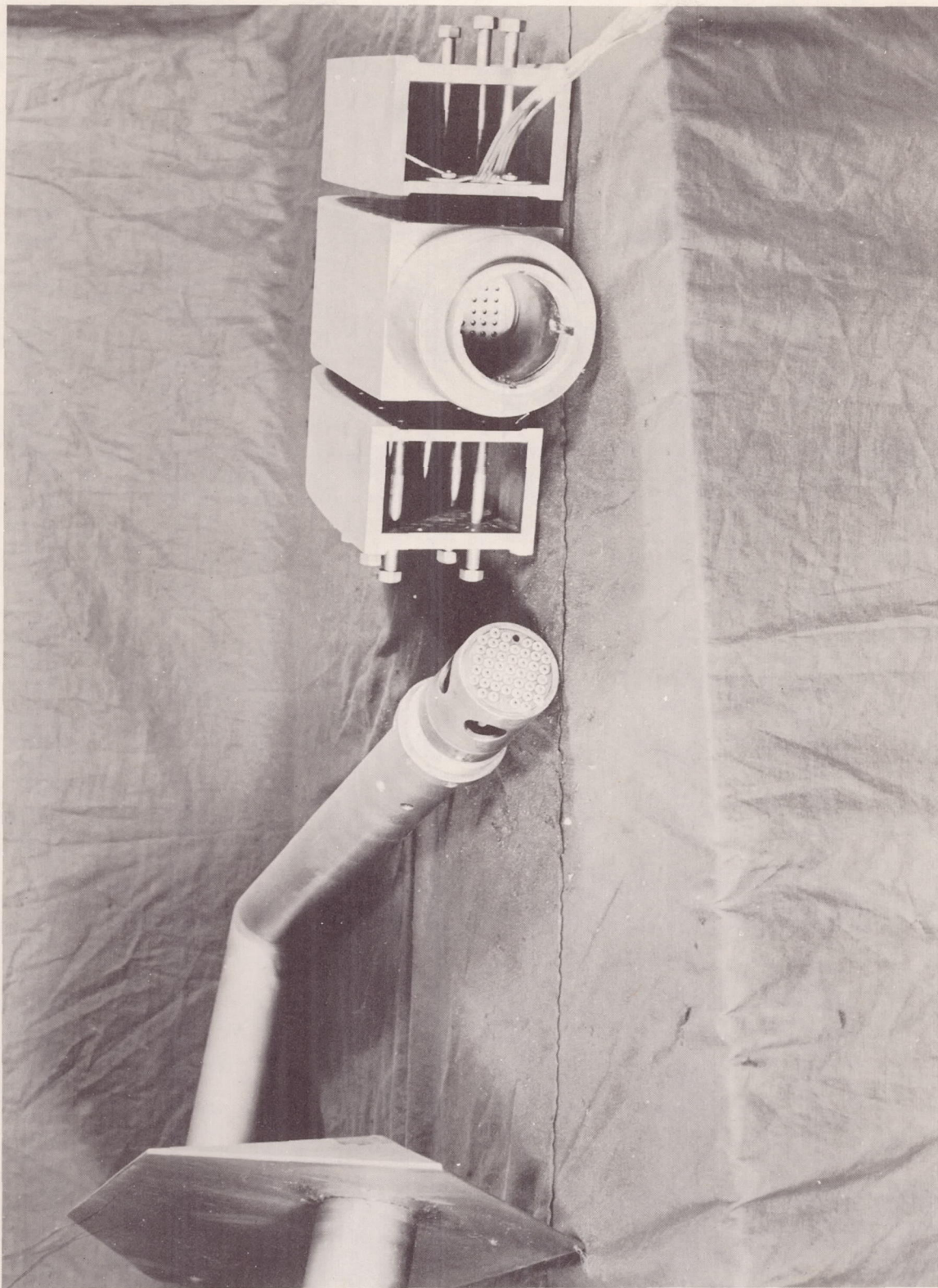
(b) Circular arc models.



(c) Wedge models.

L-63-83

25 Figure 1.- Photograph of two-dimensional aerodynamically blunt bodies.



L-62-872

Figure 2.- Photograph of 78° parabola with extensions and support.

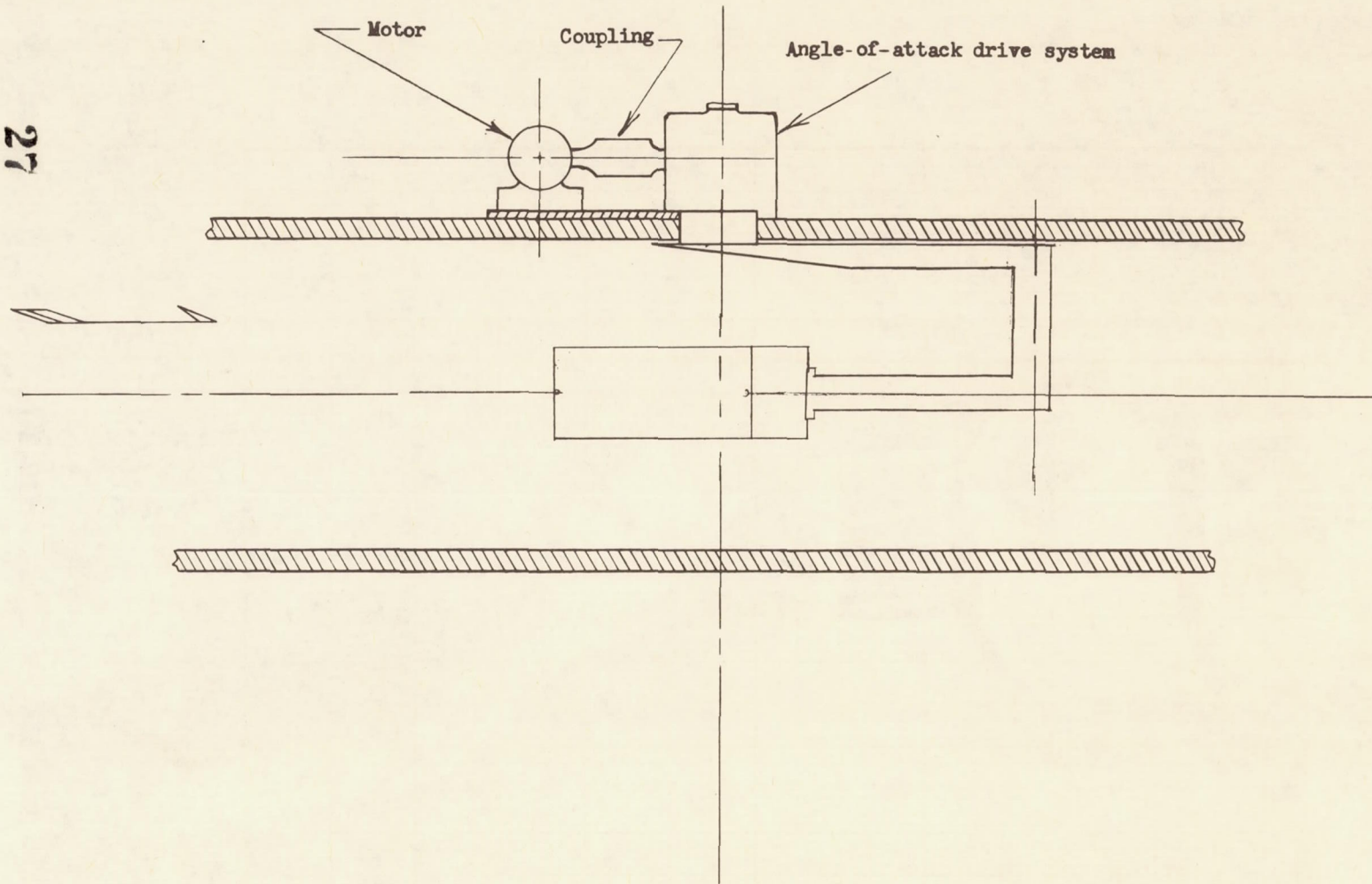


Figure 3.- Schematic diagram of model support system.

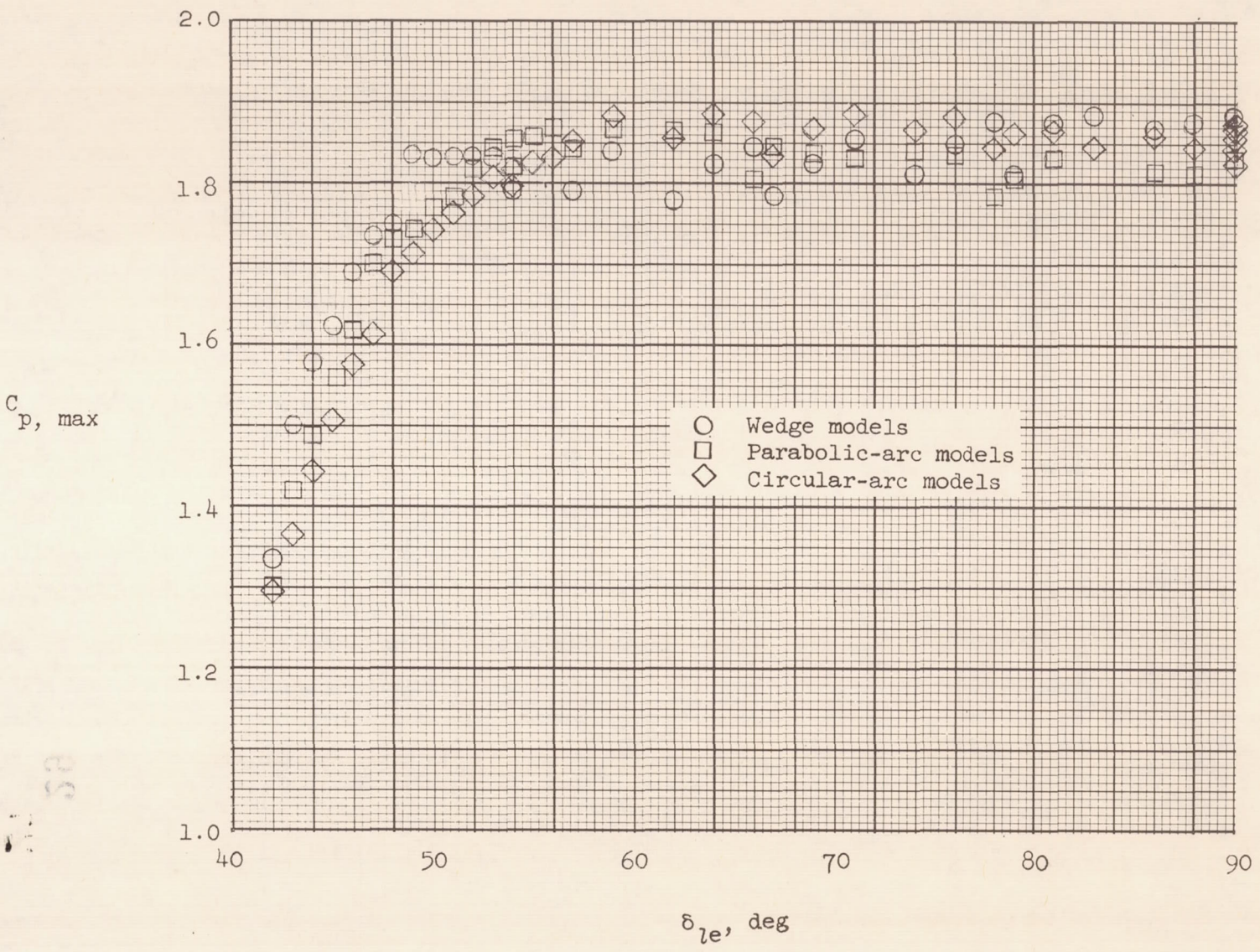


Figure 4.- Maximum pressure coefficients based upon an assumed Mach number of 6.

29

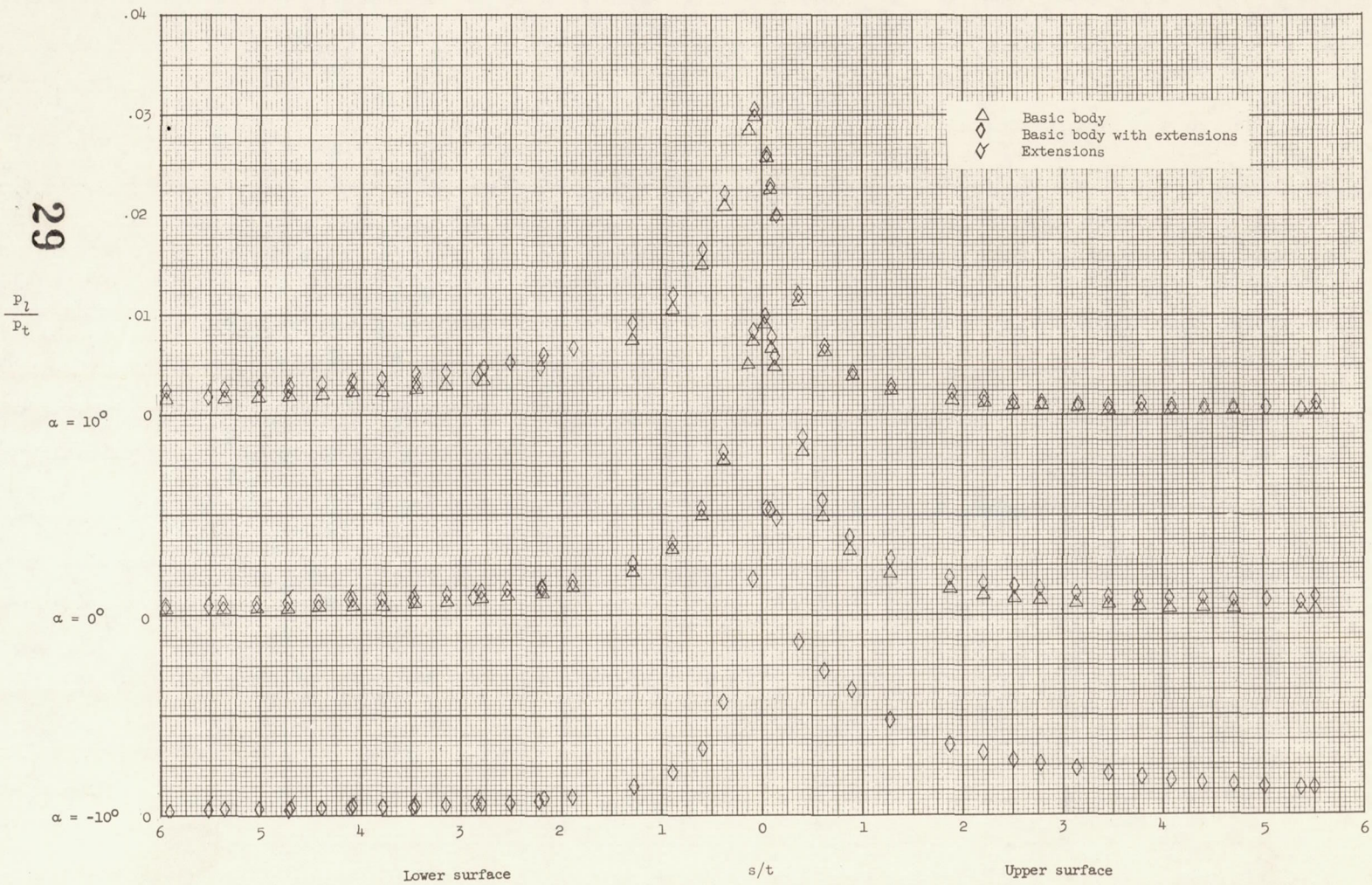
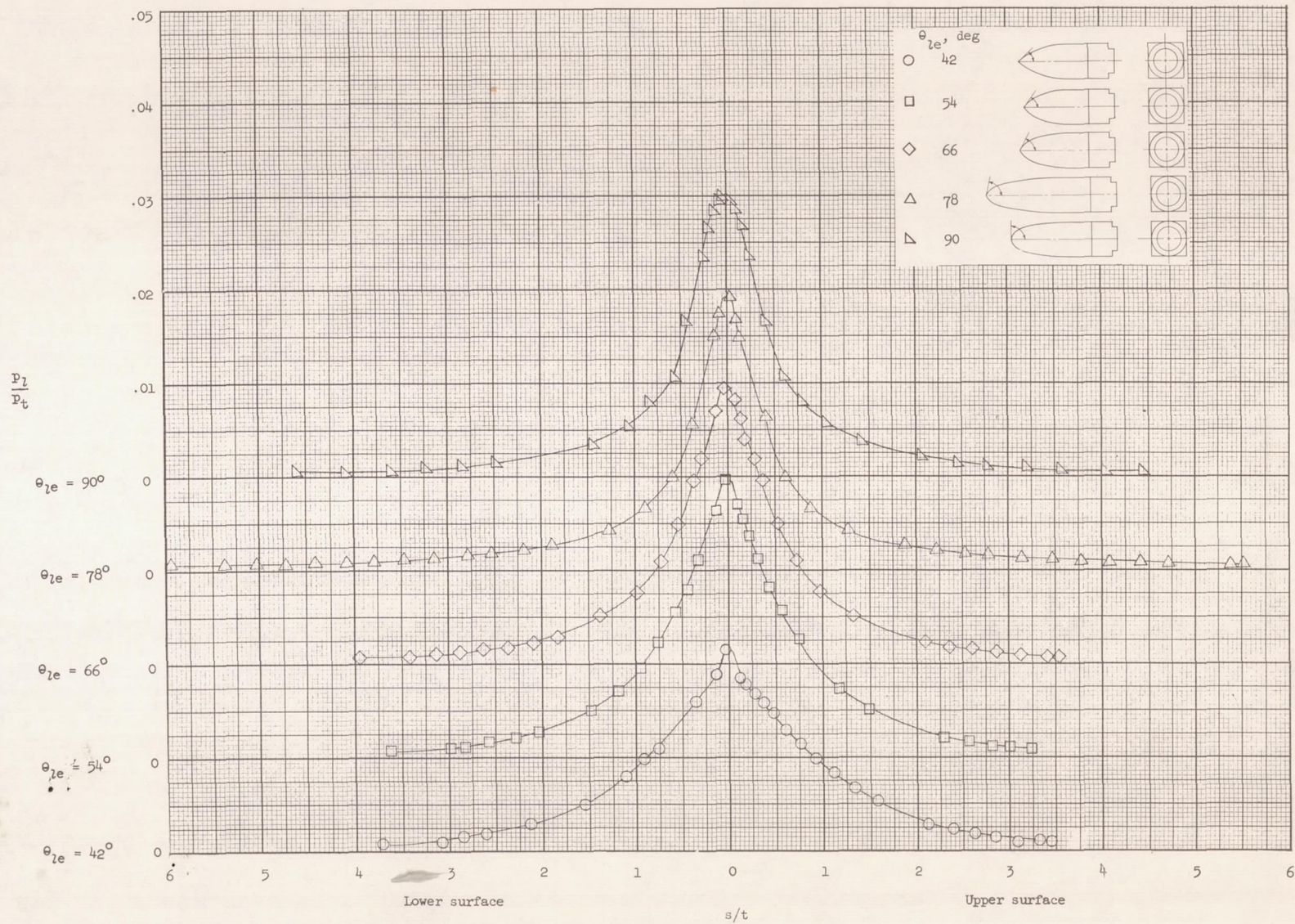


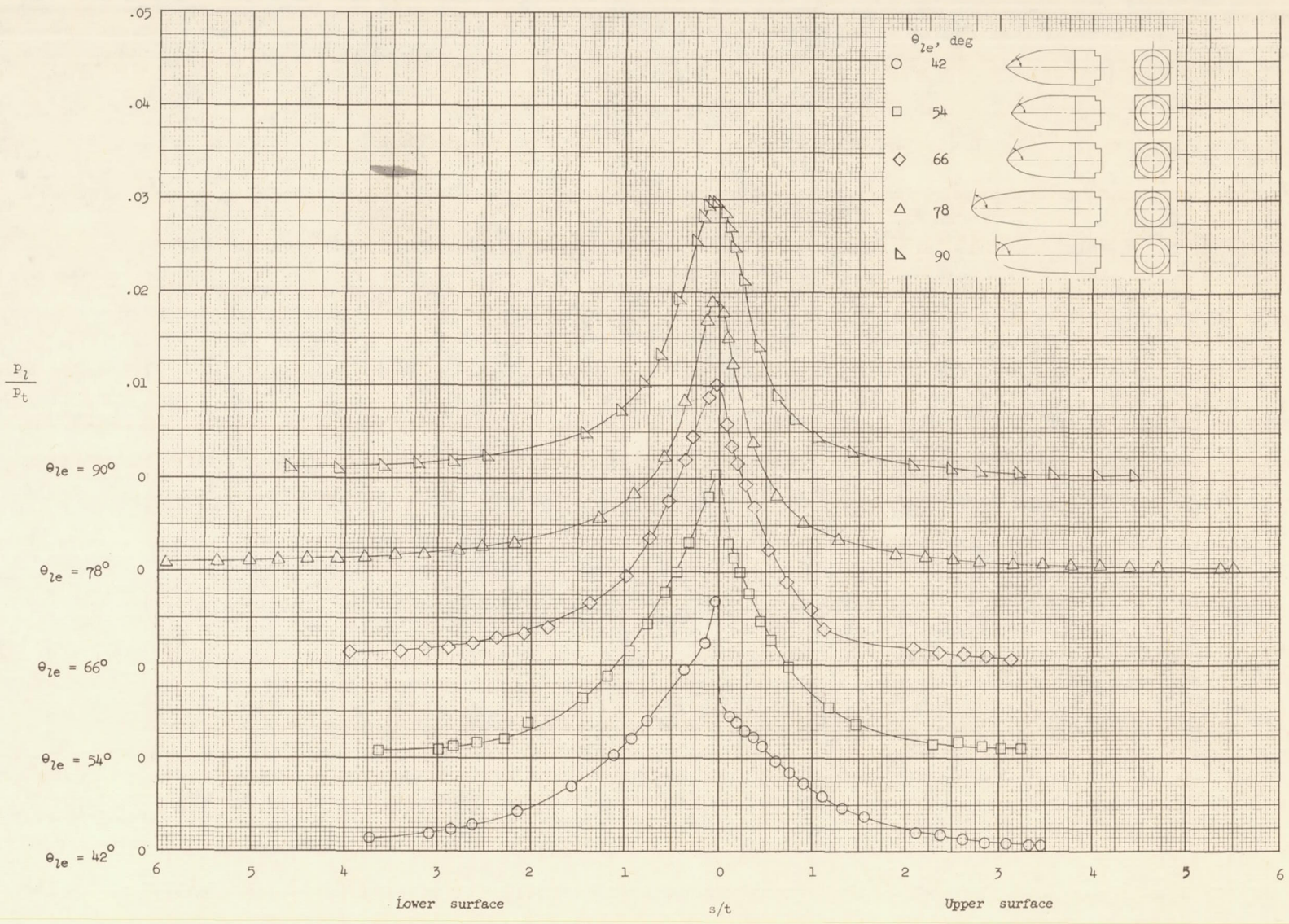
Figure 5.- Pressure distributions of two-dimensional 78° parabola with and without extensions.



(a) $\alpha = 0^\circ$.

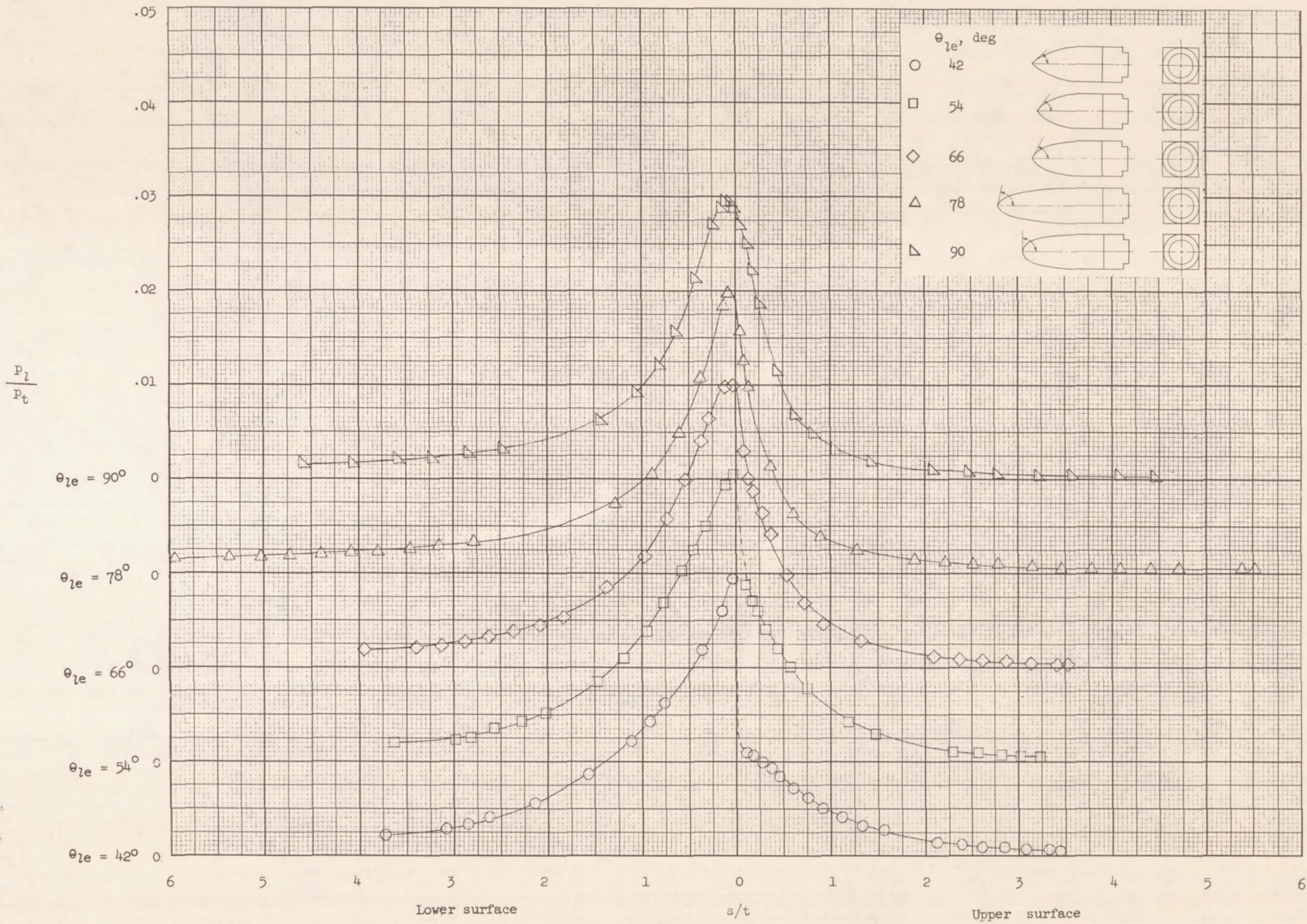
Figure 6.- Pressure distributions of two-dimensional parabolas.

30
08
31



(b) $\alpha = 5^\circ$.

Figure 6.- Continued.



(c) $\alpha = 10^\circ$.

Figure 6.- Continued.

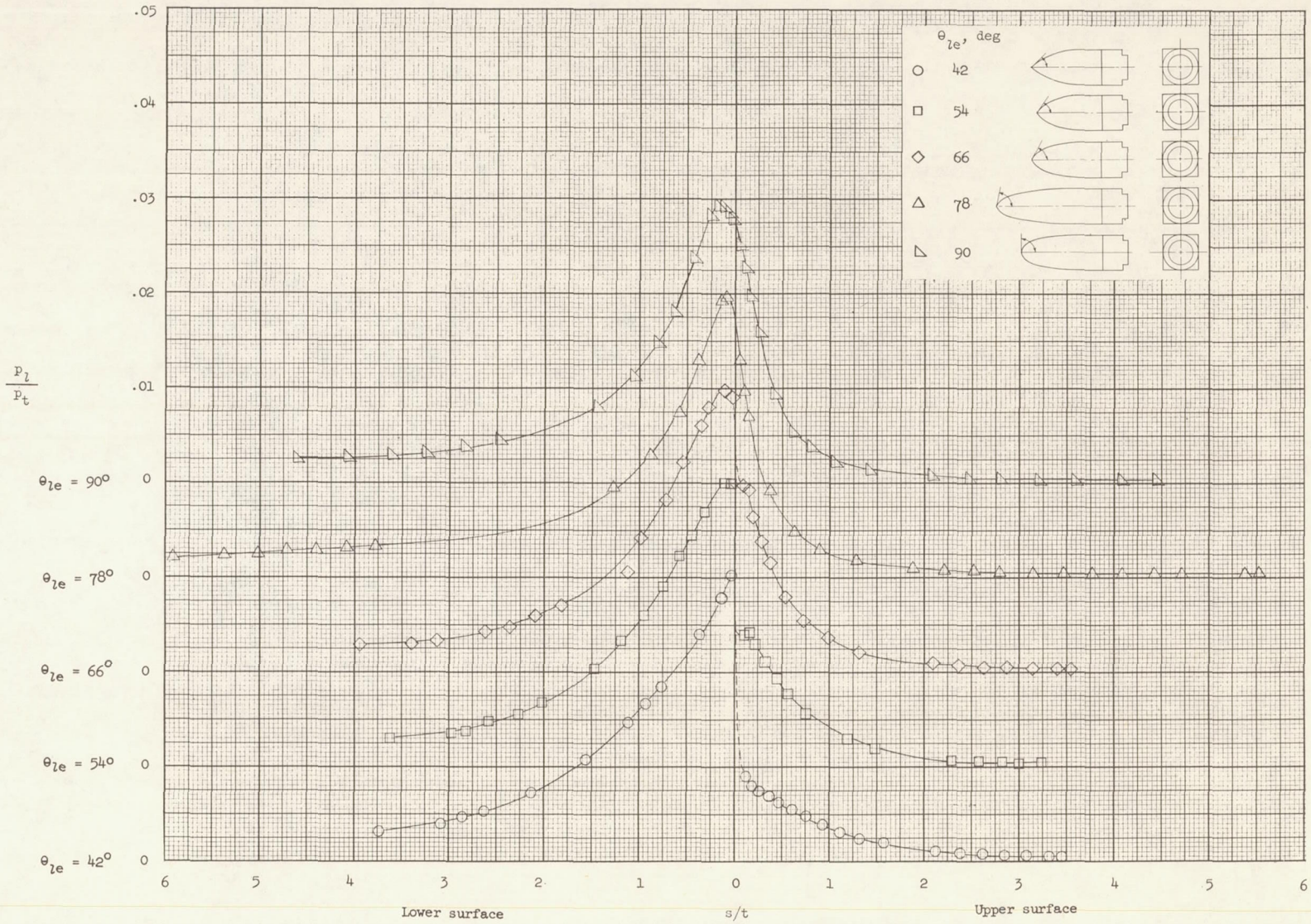
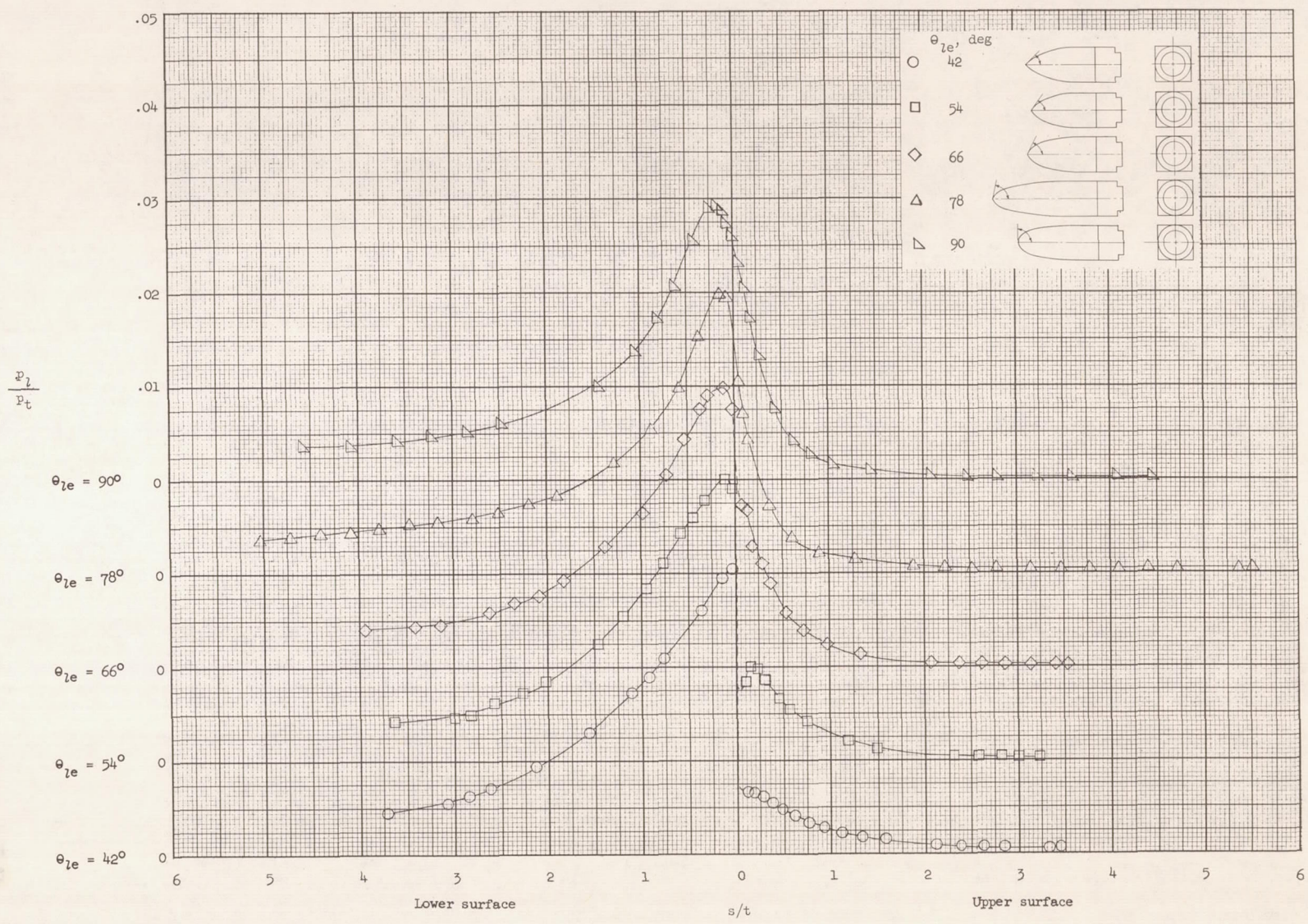
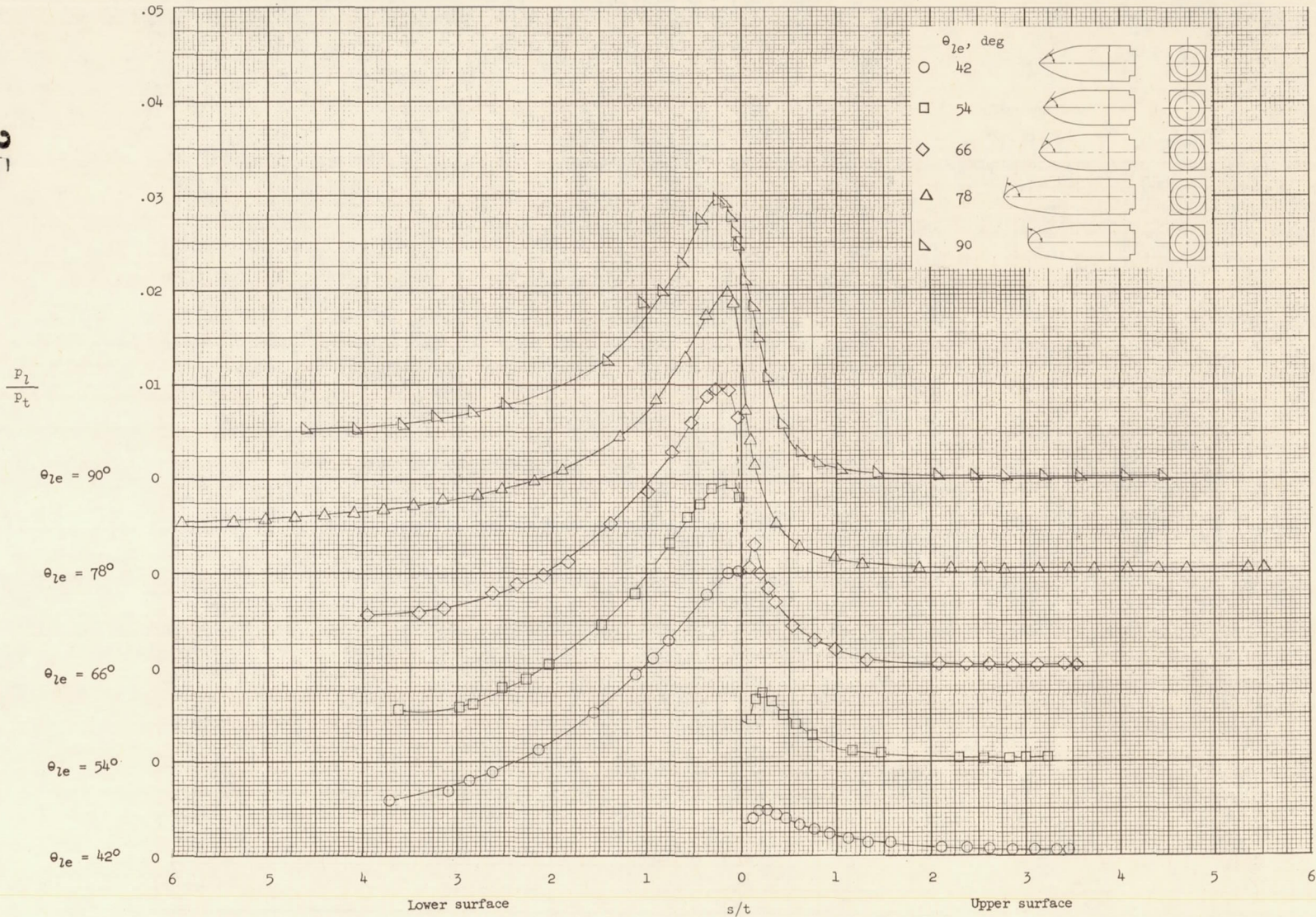


Figure 6.- Continued.



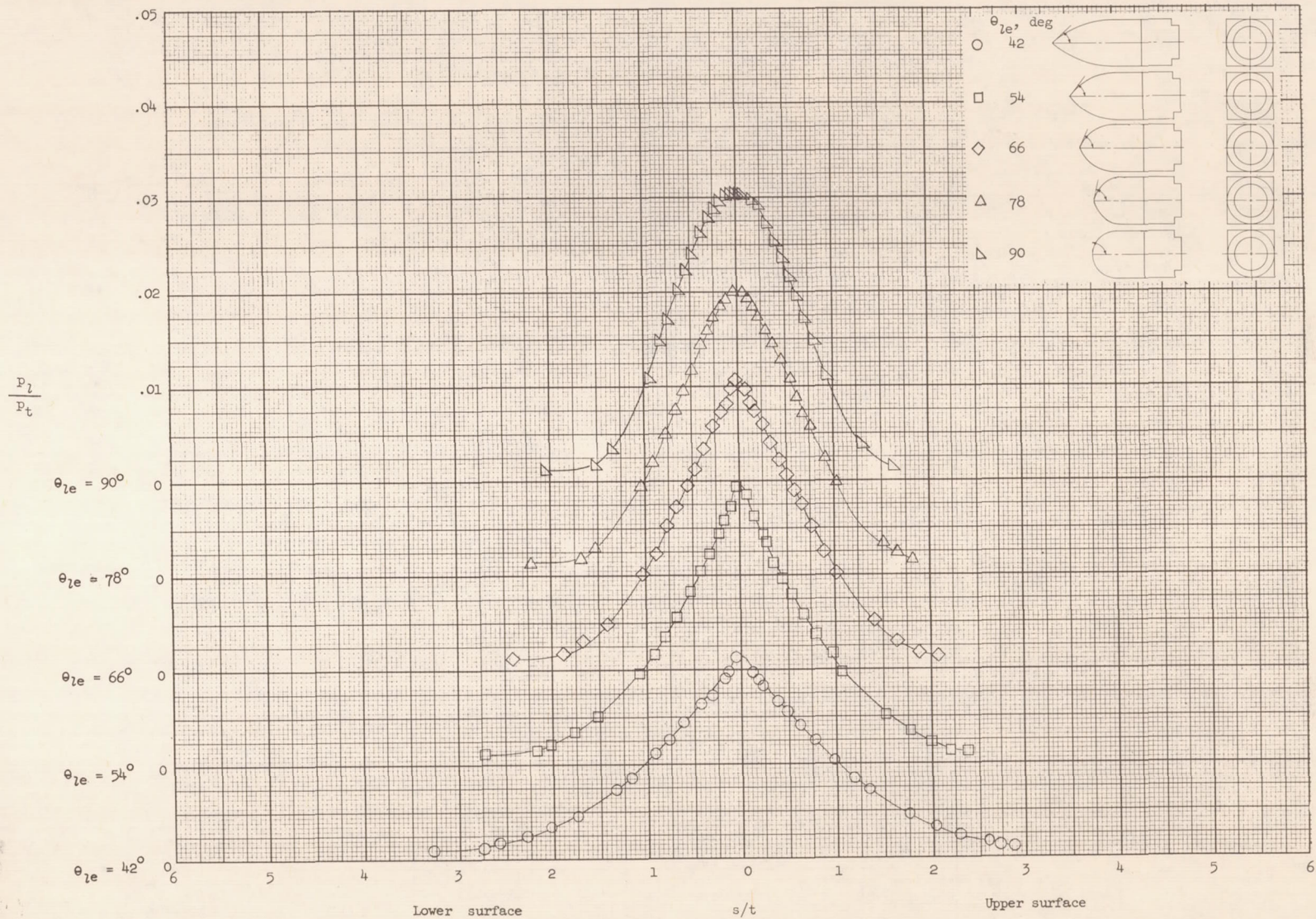
(e) $\alpha = 20^\circ$.

Figure 6.- Continued.



(f) $\alpha = 25^\circ$.

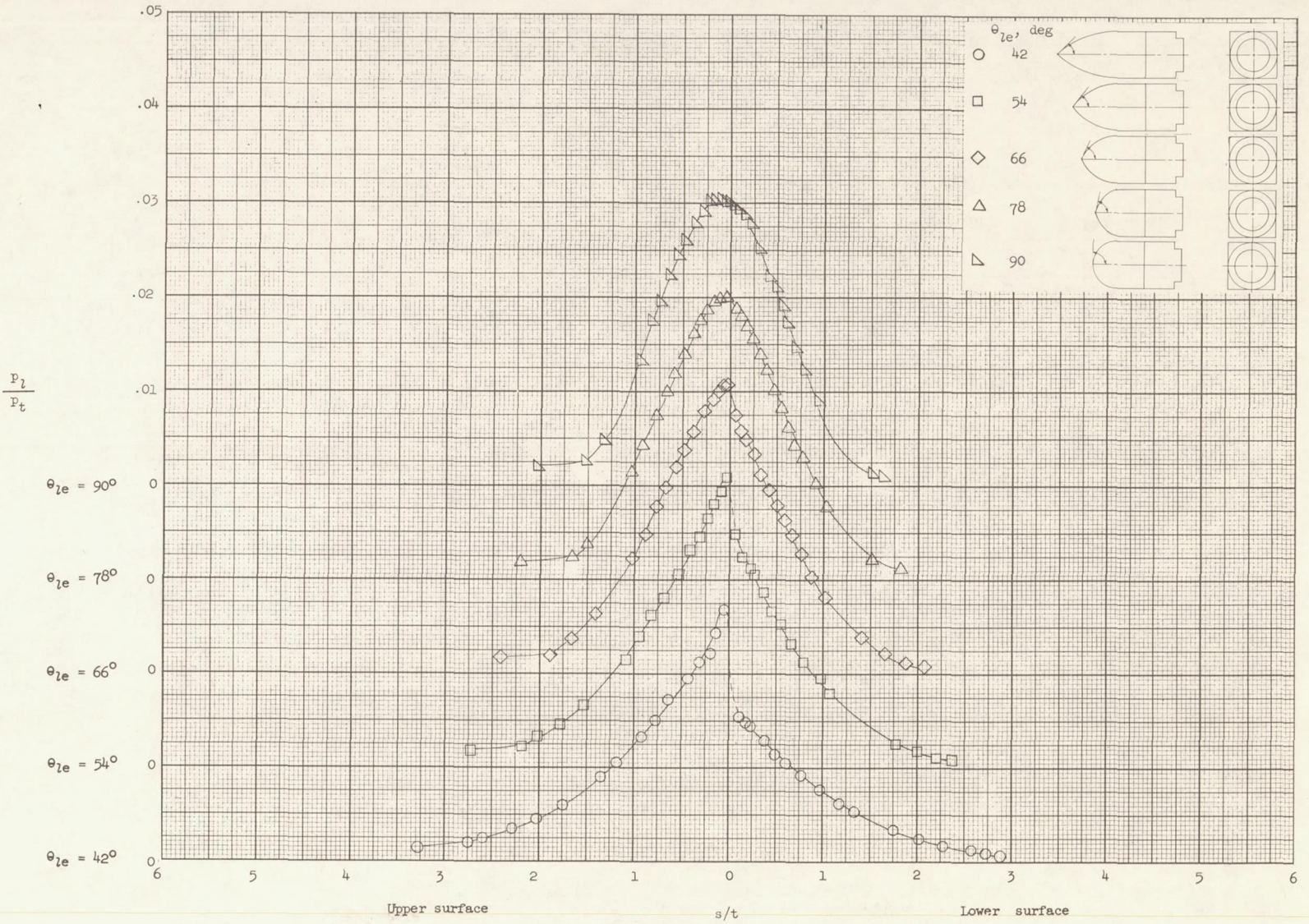
Figure 6.- Concluded.



(a) $\alpha = 0^\circ$.

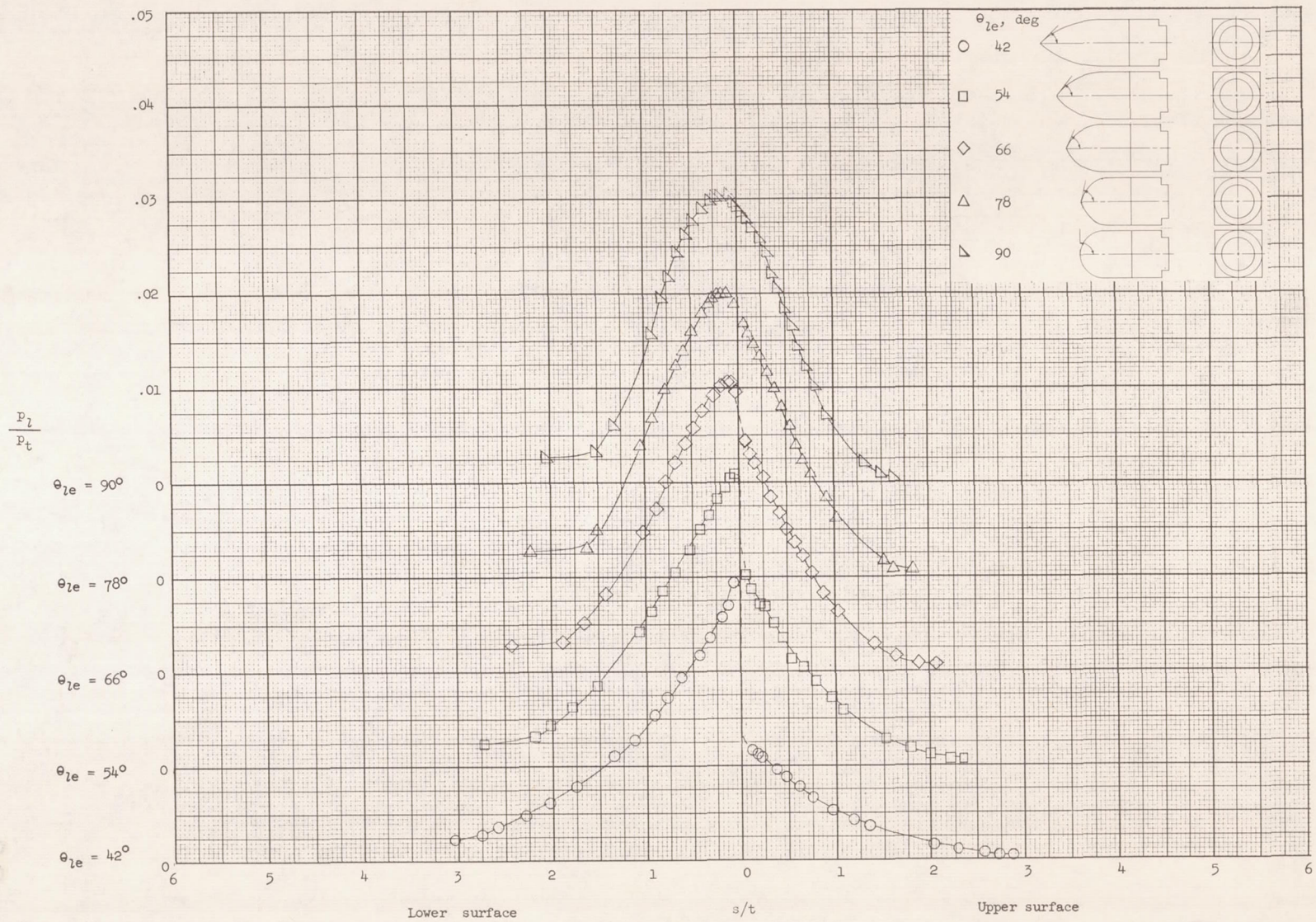
Figure 7.- Pressure distributions of two-dimensional circular arcs.

36



(b) $\alpha = 5^\circ$.

Figure 7.- Continued.

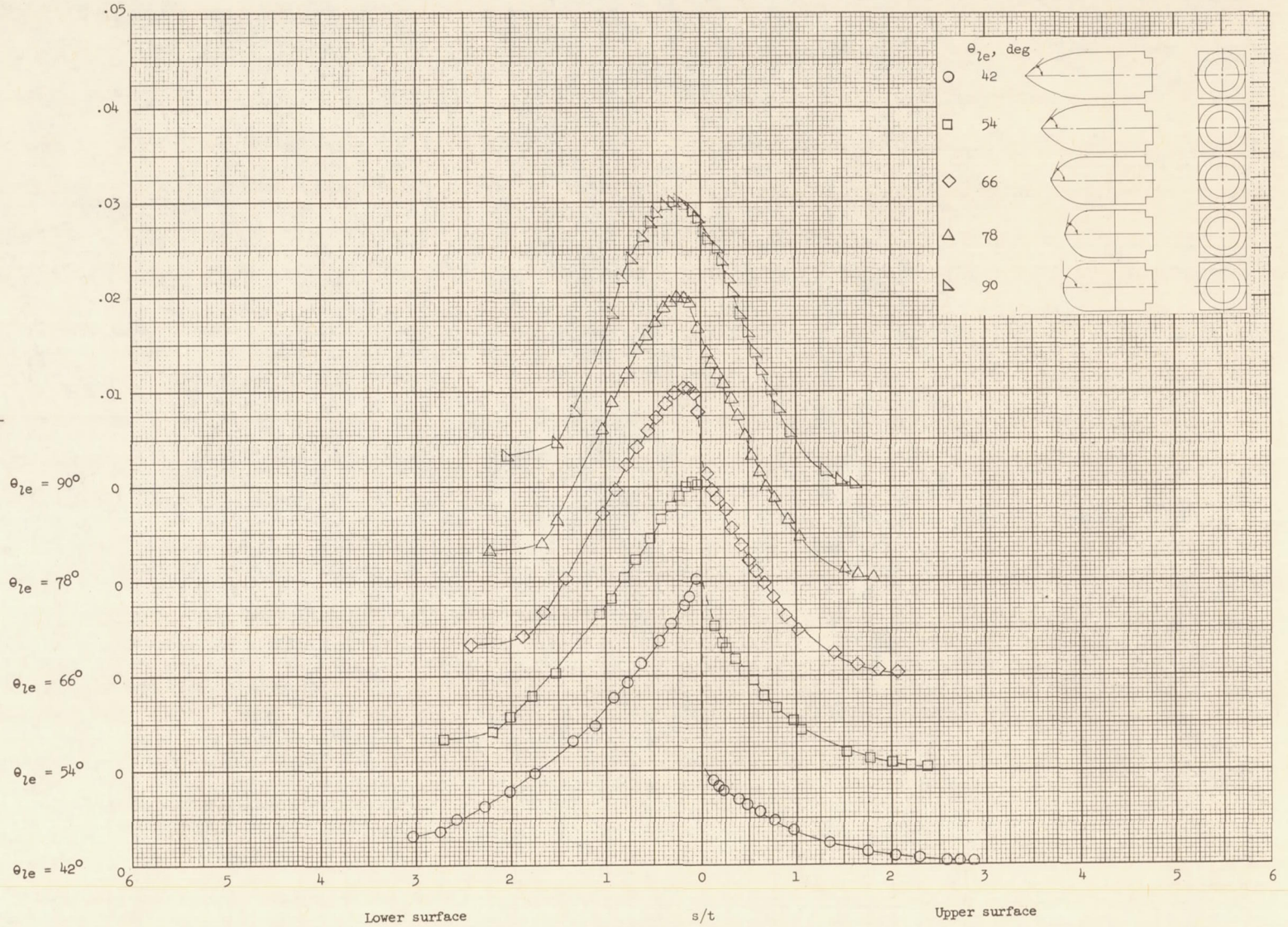


(c) $\alpha = 10^\circ$.

Figure 7.- Continued.

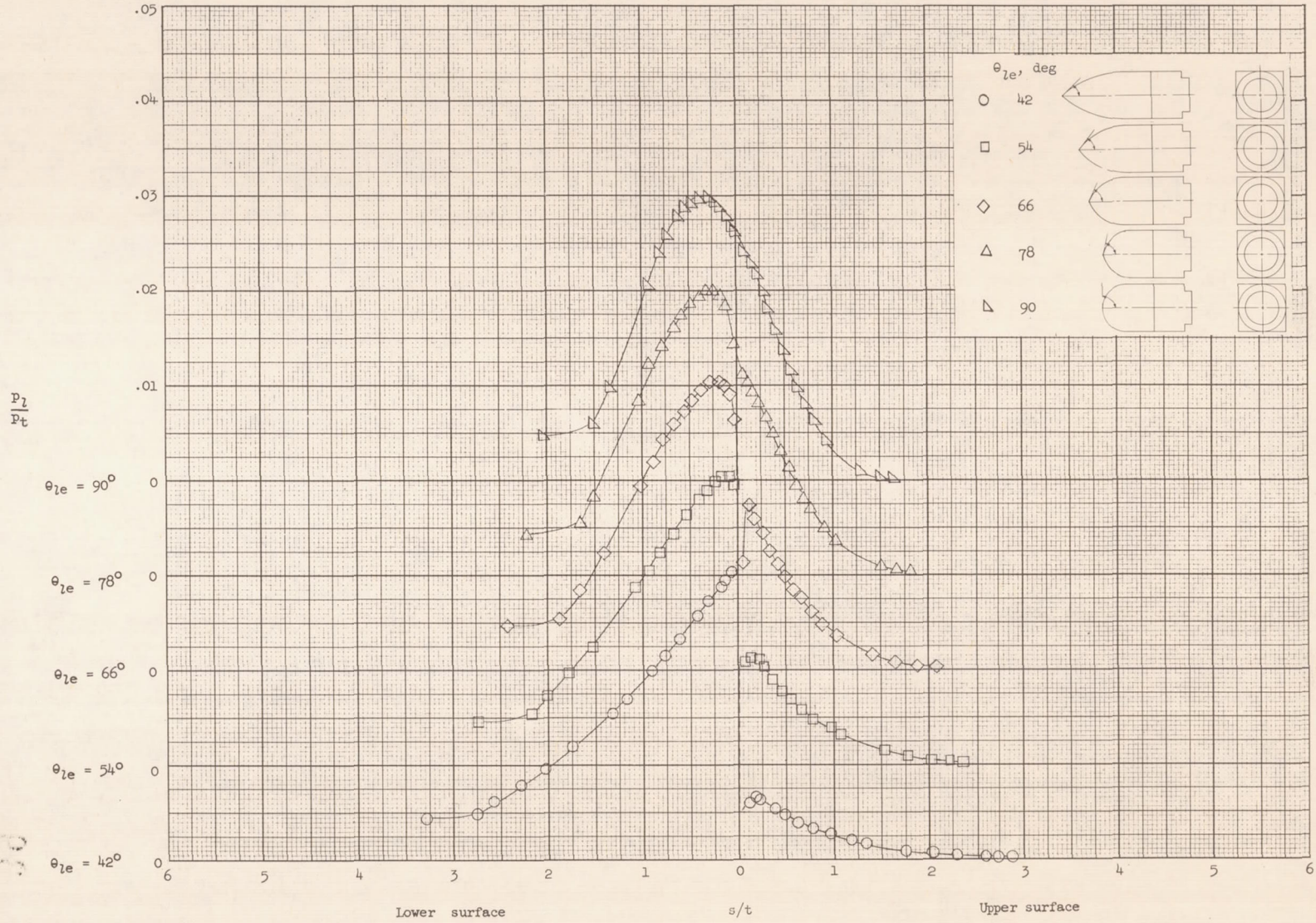
38

$$\frac{P_i}{P_t}$$



(d) $\alpha = 15^\circ$.

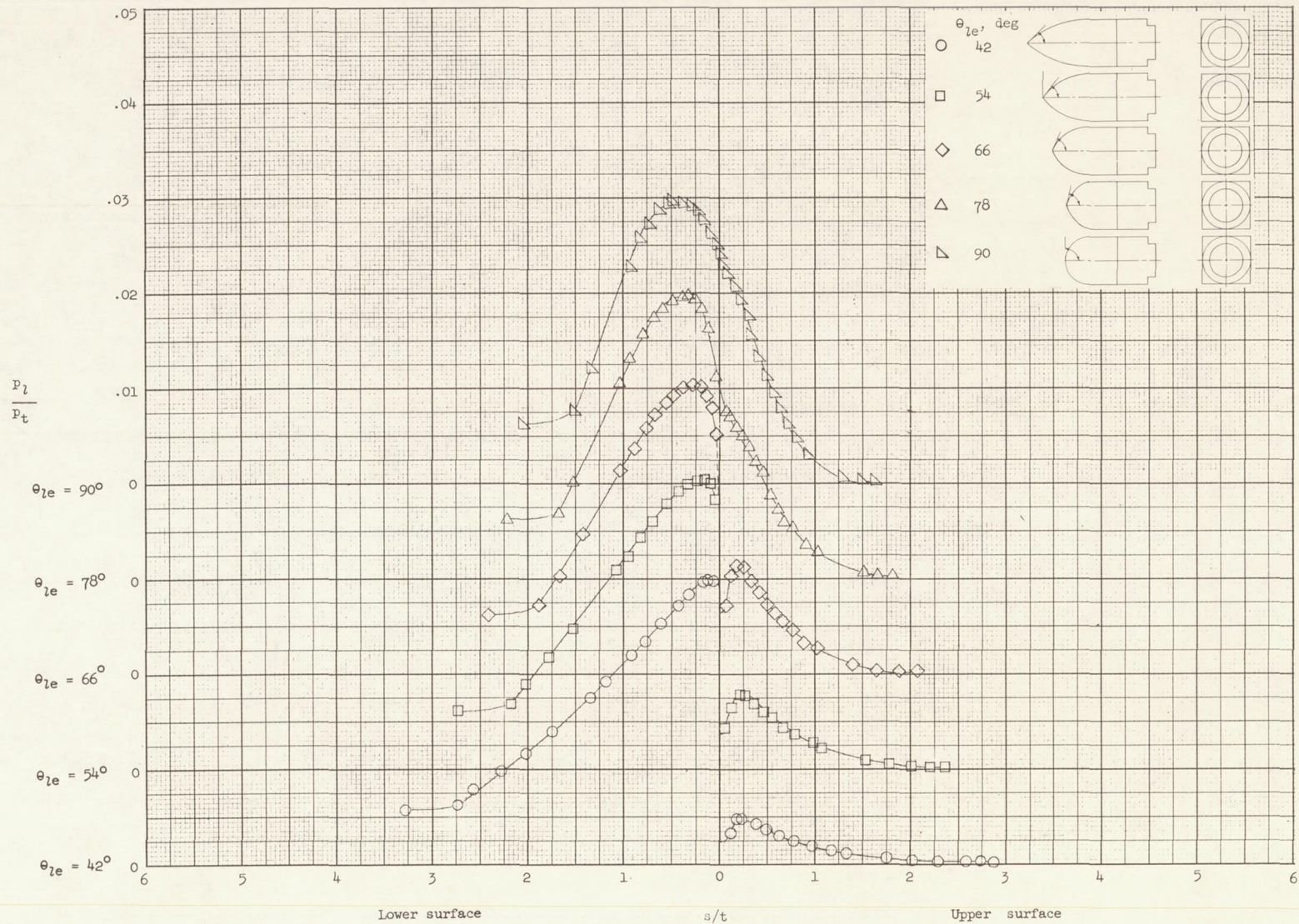
Figure 7.- Continued.



(e) $\alpha = 20^\circ$.

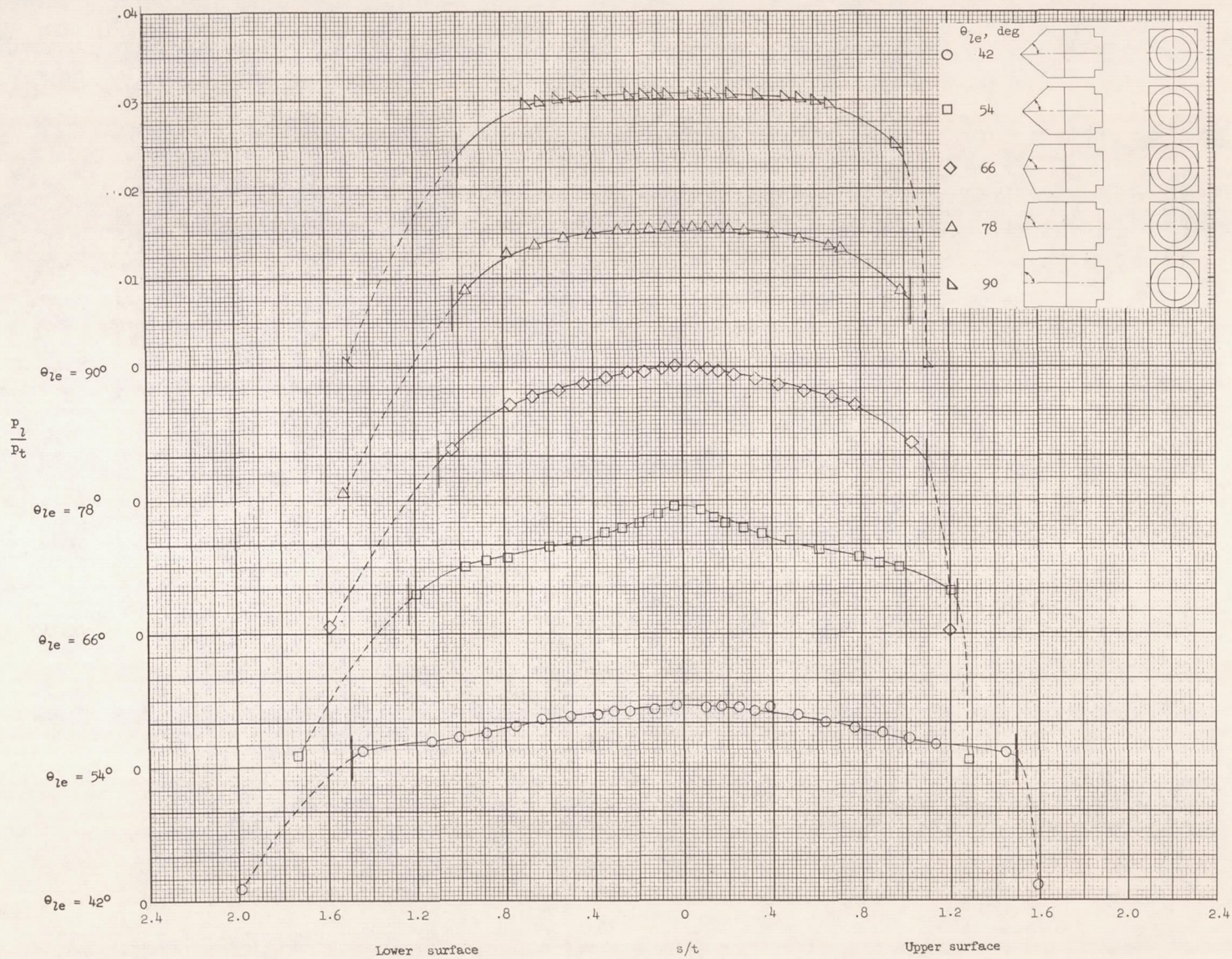
Figure 7.- Continued.

1140



(f) $\alpha = 25^\circ$.

Figure 7.- Concluded.

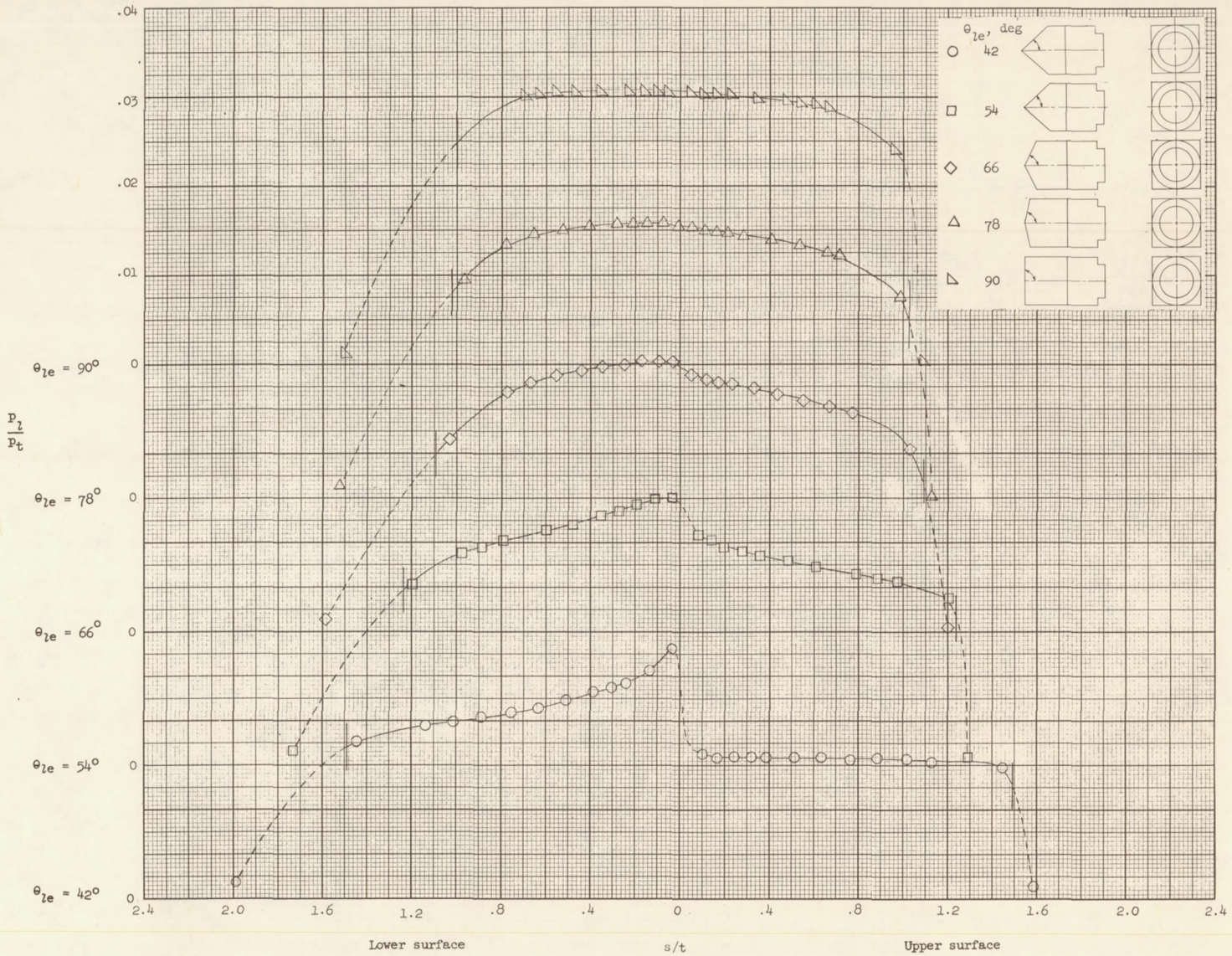


(a) $\alpha = 0^\circ$.

Figure 8.- Pressure distributions of wedges.

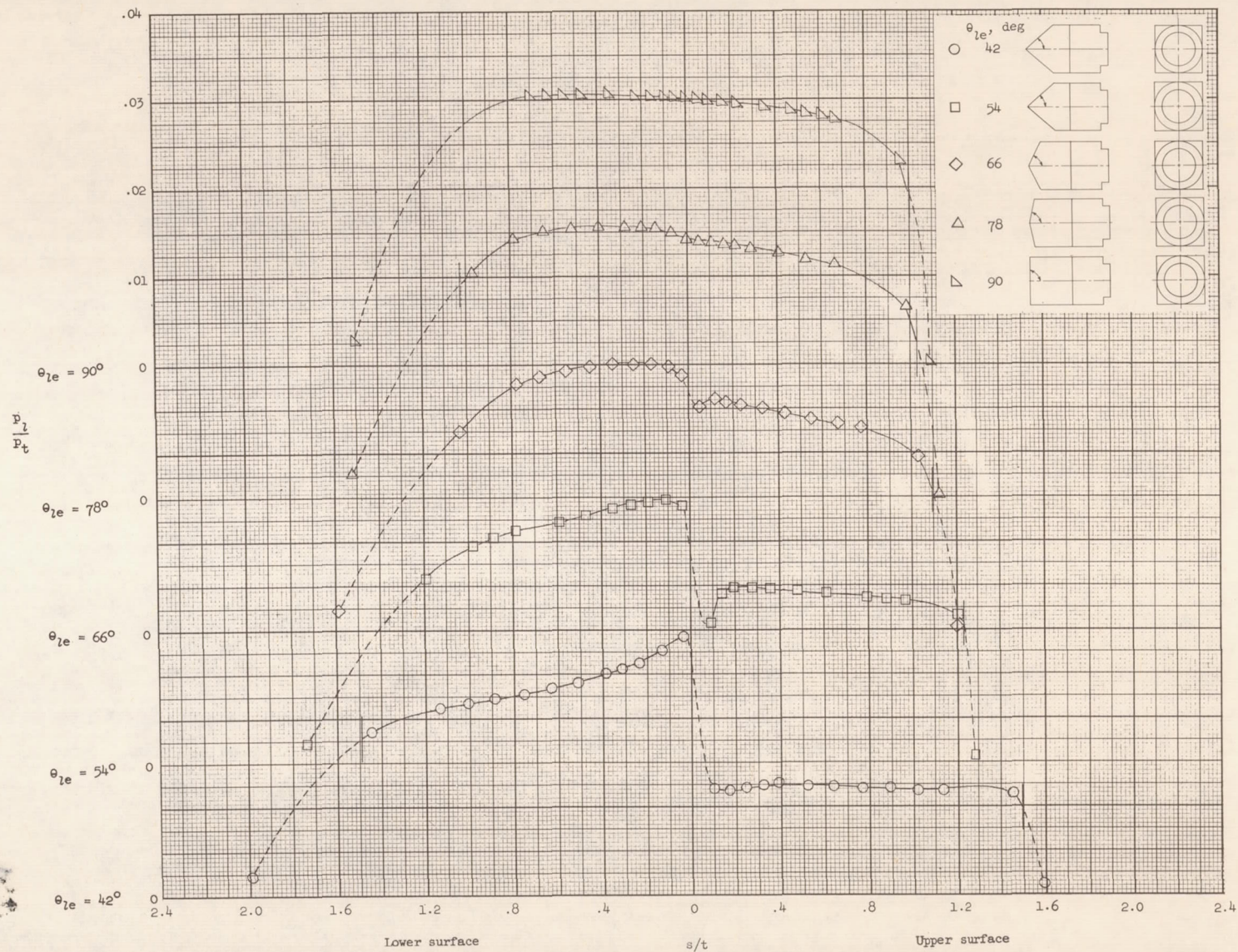
142

17



(b) $\alpha = 5^\circ$.

Figure 8.- Continued.

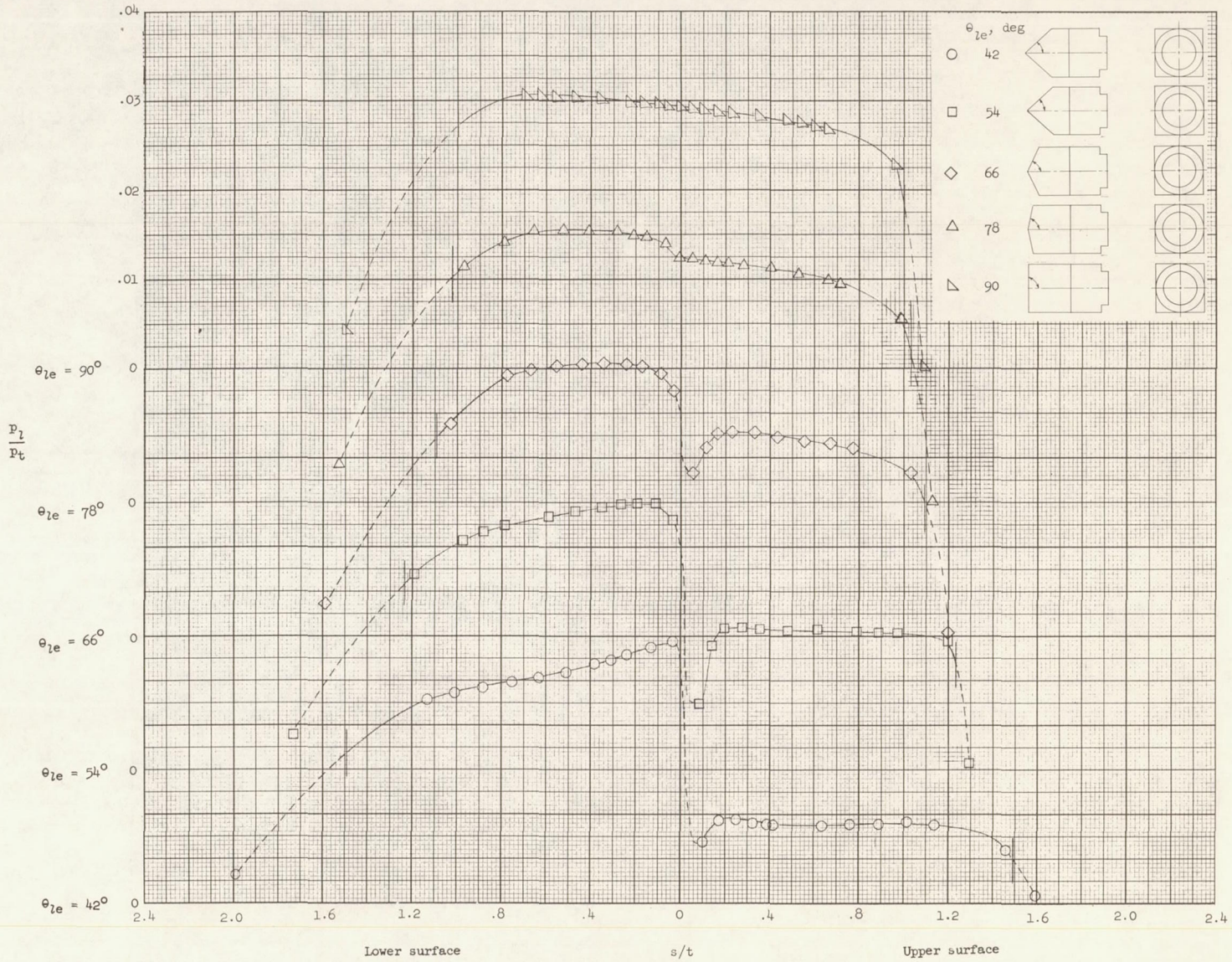


(c) $\alpha = 10^\circ$.

Figure 8.- Continued.

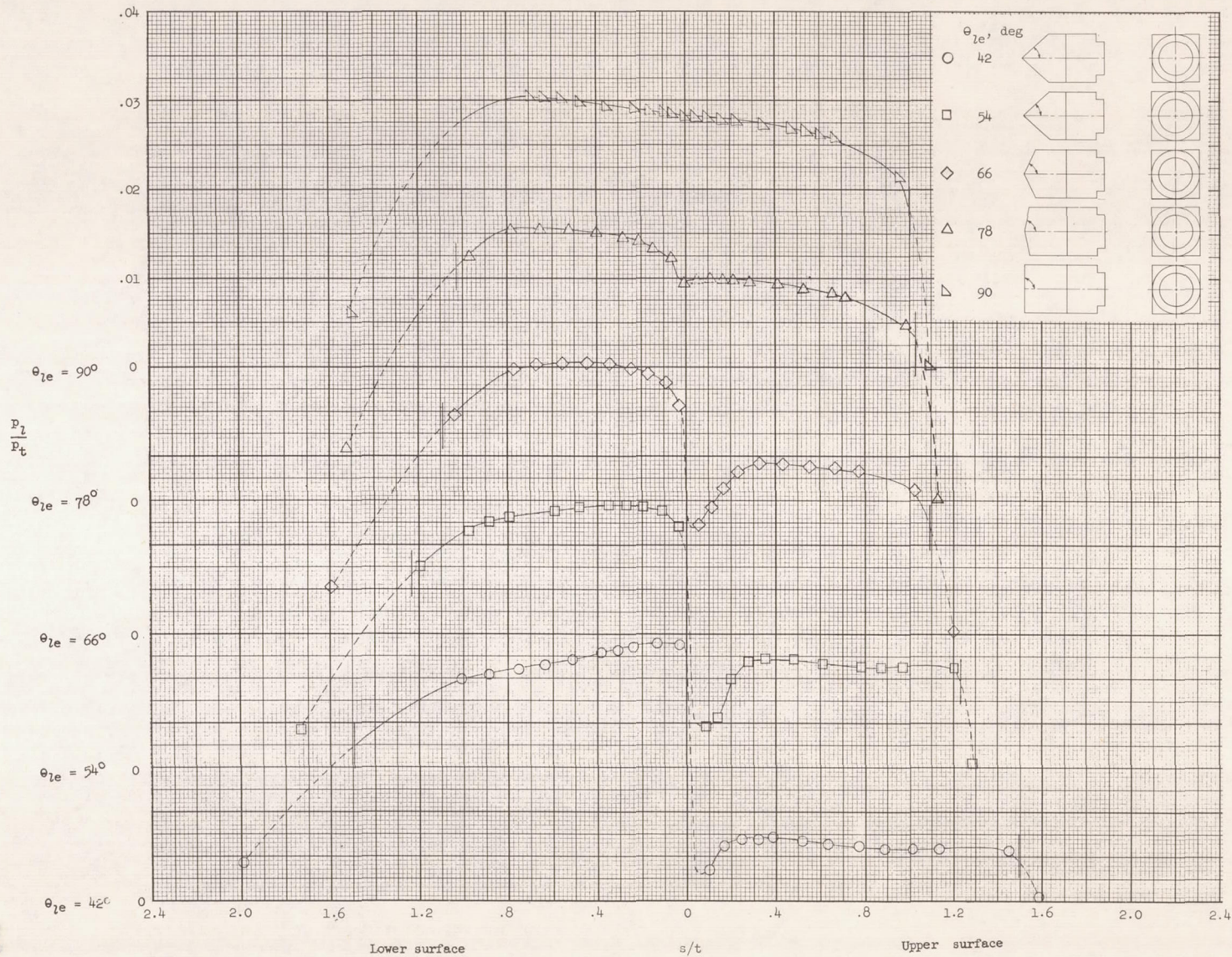
41

43



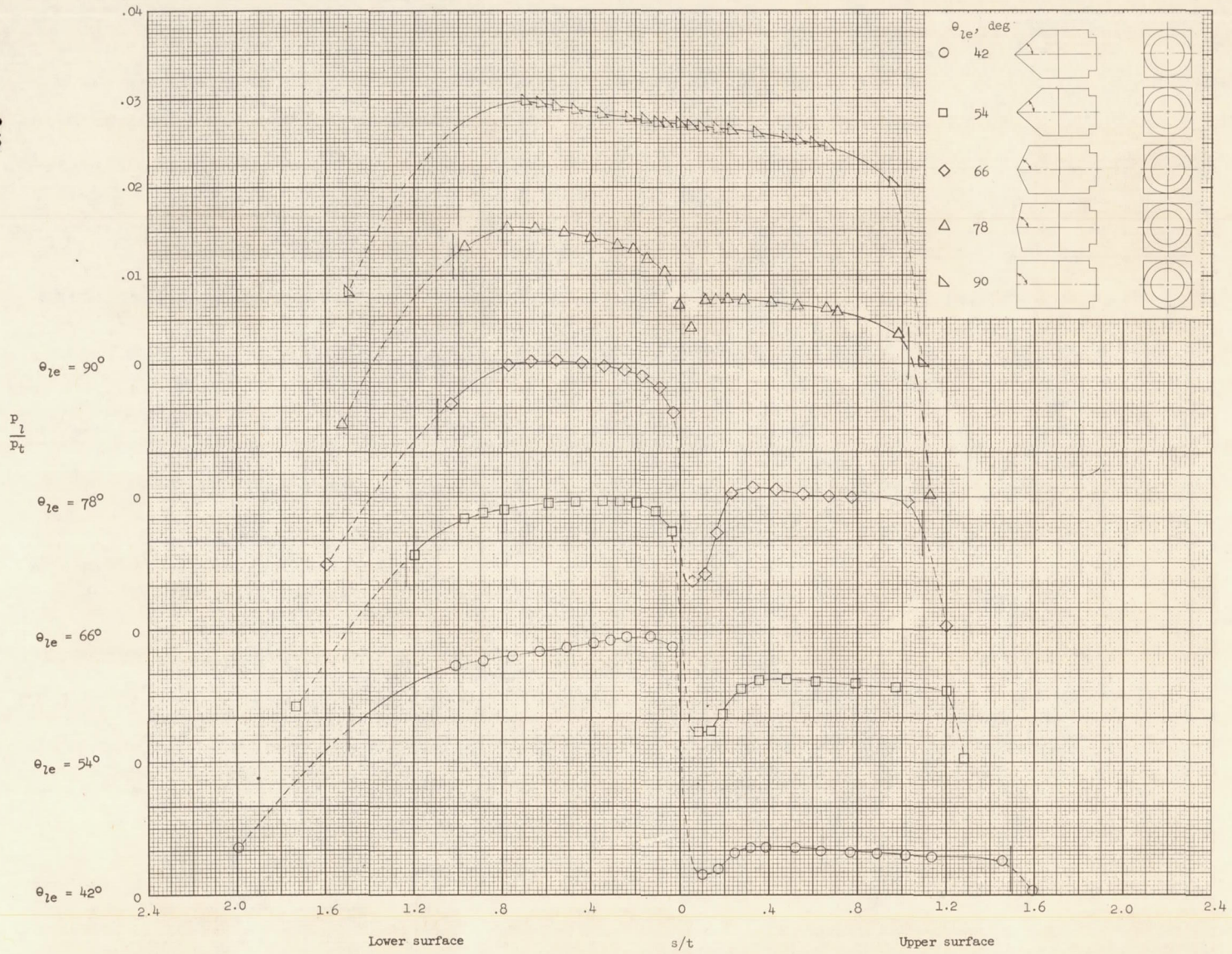
(d) $\alpha = 15^\circ$.

Figure 8.- Continued.



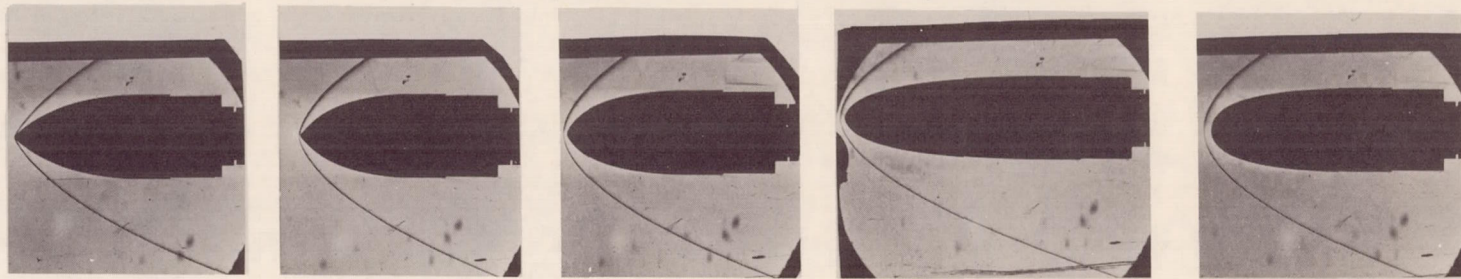
(e) $\alpha = 20^\circ$.

Figure 8.- Continued.



(f) $\alpha = 25^\circ$.

Figure 8.- Concluded.



$\theta_{le} = 42^\circ$

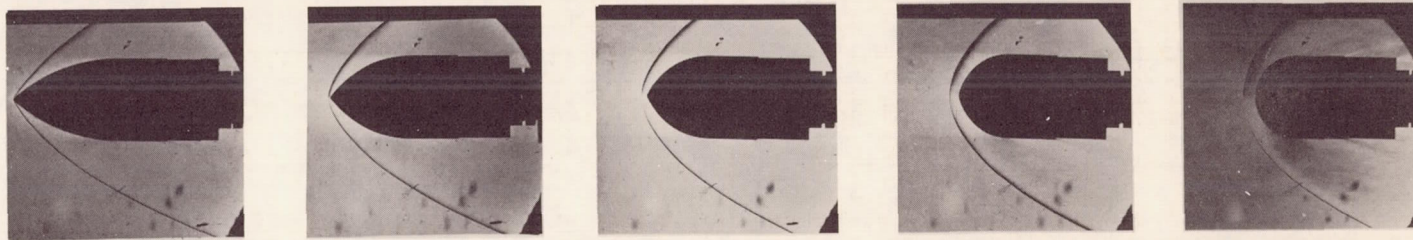
$\theta_{le} = 54^\circ$

$\theta_{le} = 66^\circ$

$\theta_{le} = 78^\circ$

$\theta_{le} = 90^\circ$

(a) Parabolic arc models.



$\theta_{le} = 42^\circ$

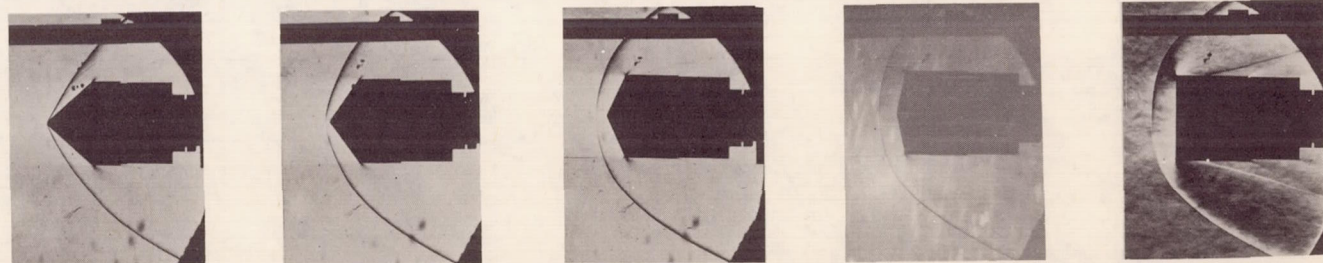
$\theta_{le} = 54^\circ$

$\theta_{le} = 66^\circ$

$\theta_{le} = 78^\circ$

$\theta_{le} = 90^\circ$

(b) Circular arc models.



$\theta_{le} = 42^\circ$

$\theta_{le} = 54^\circ$

$\theta_{le} = 66^\circ$

$\theta_{le} = 78^\circ$

$\theta_{le} = 90^\circ$

(c) Wedge models.

L-63-82

Figure 9.- Schlieren photographs of aerodynamically blunt bodies near 0° angle of attack.

48

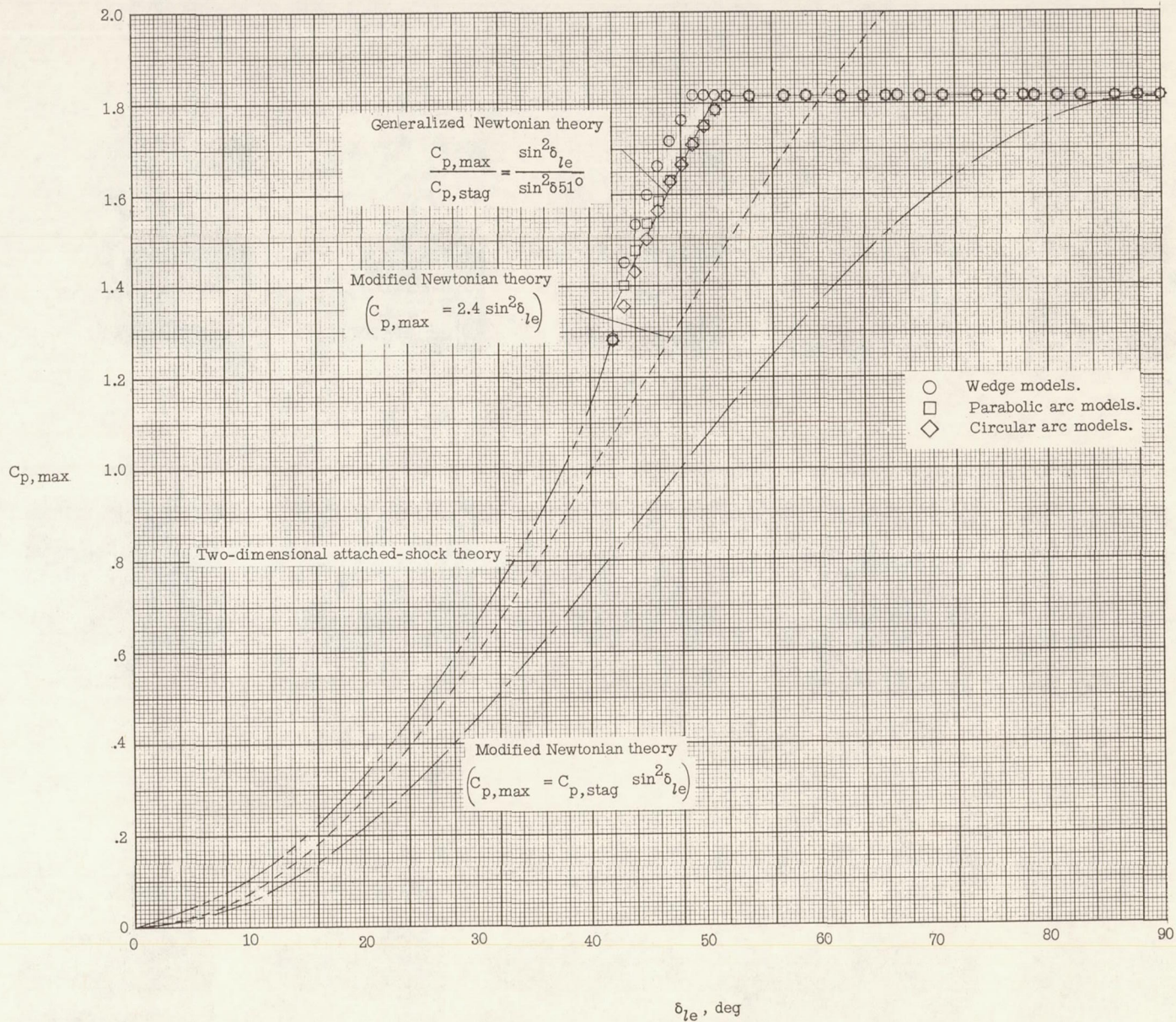
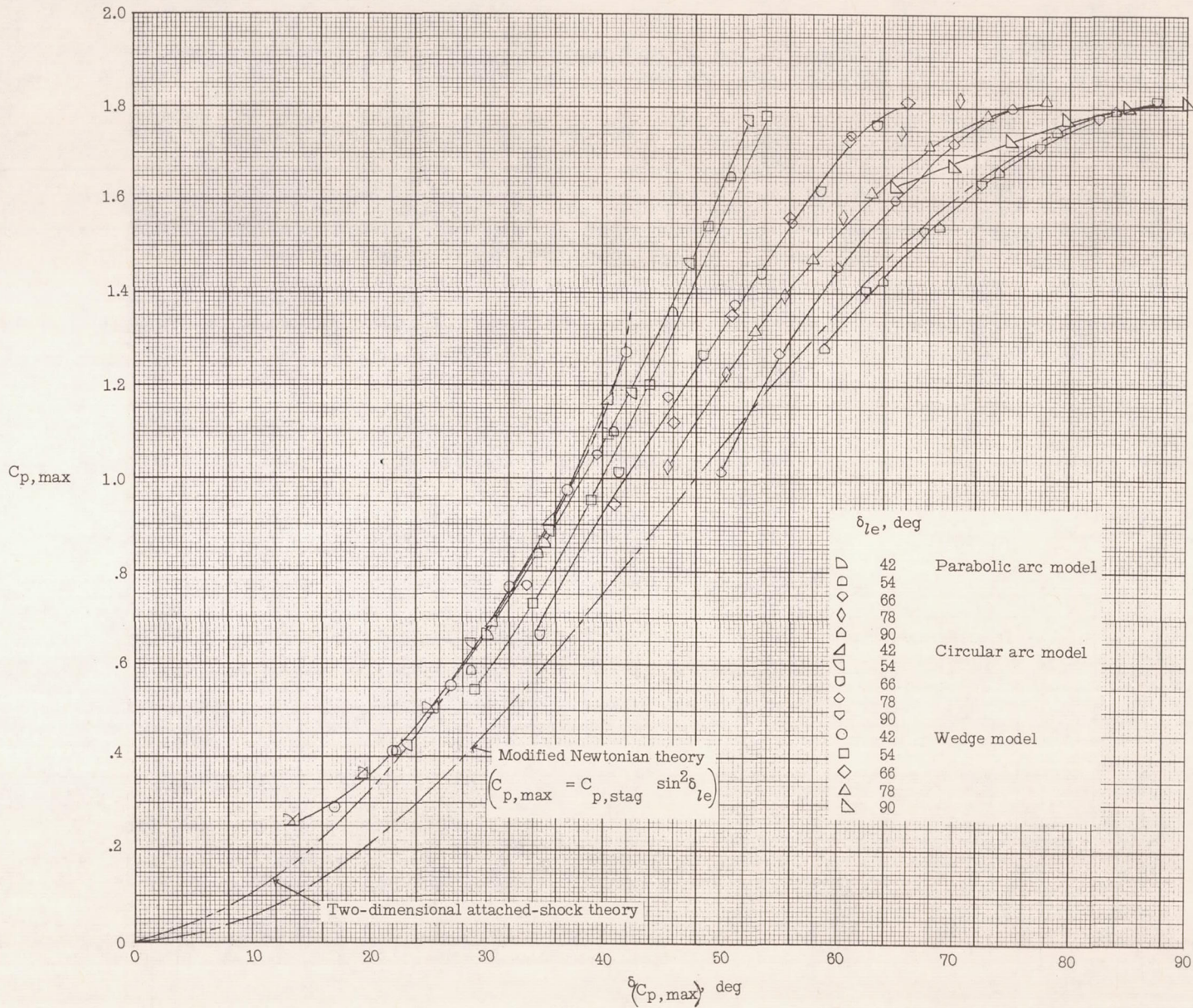
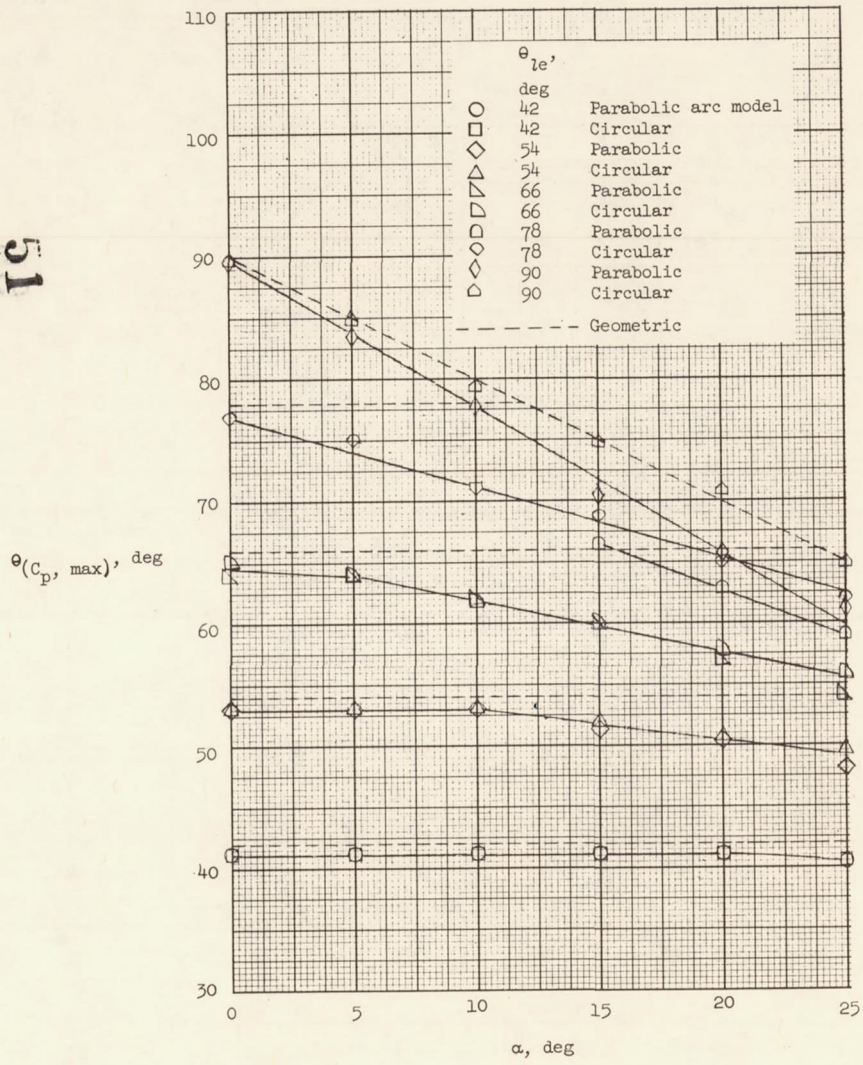


Figure 10.- Comparison of measured and predicted pressure coefficients on the lower surface for aerodynamically blunt bodies.

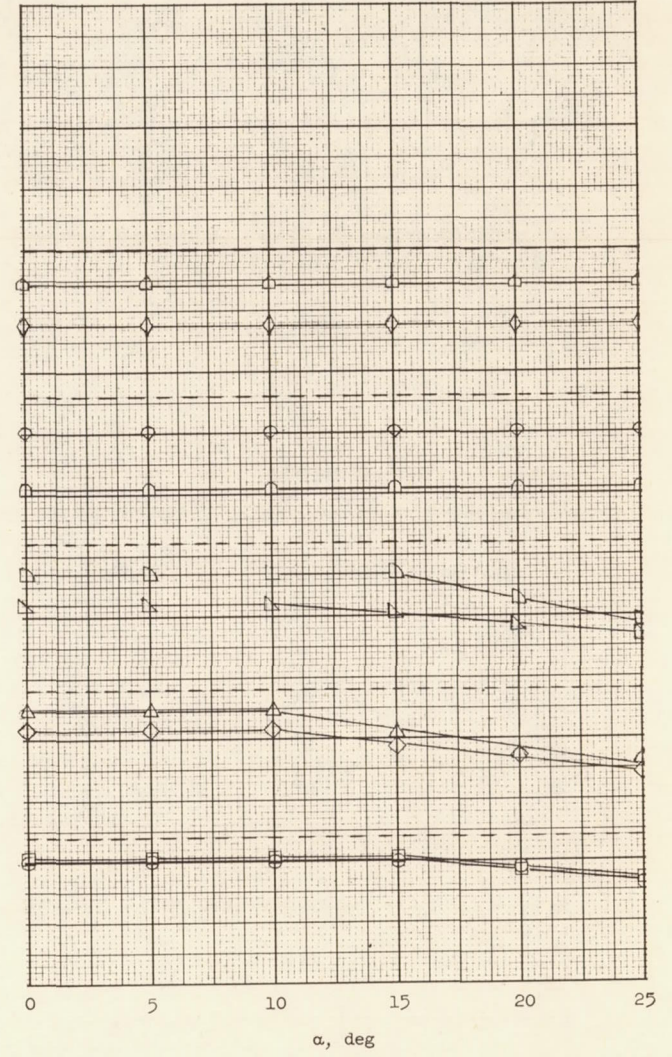
50



67 Figure 11.- Comparison measured and predicted maximum pressure coefficients on the upper surface for aerodynamically blunt bodies.



(a) Lower surface



(b) Upper surface

Figure 12.- Comparison of geometric and measured slopes at which maximum pressure occurred for various angles of attack on the parabolic and circular arc bodies.

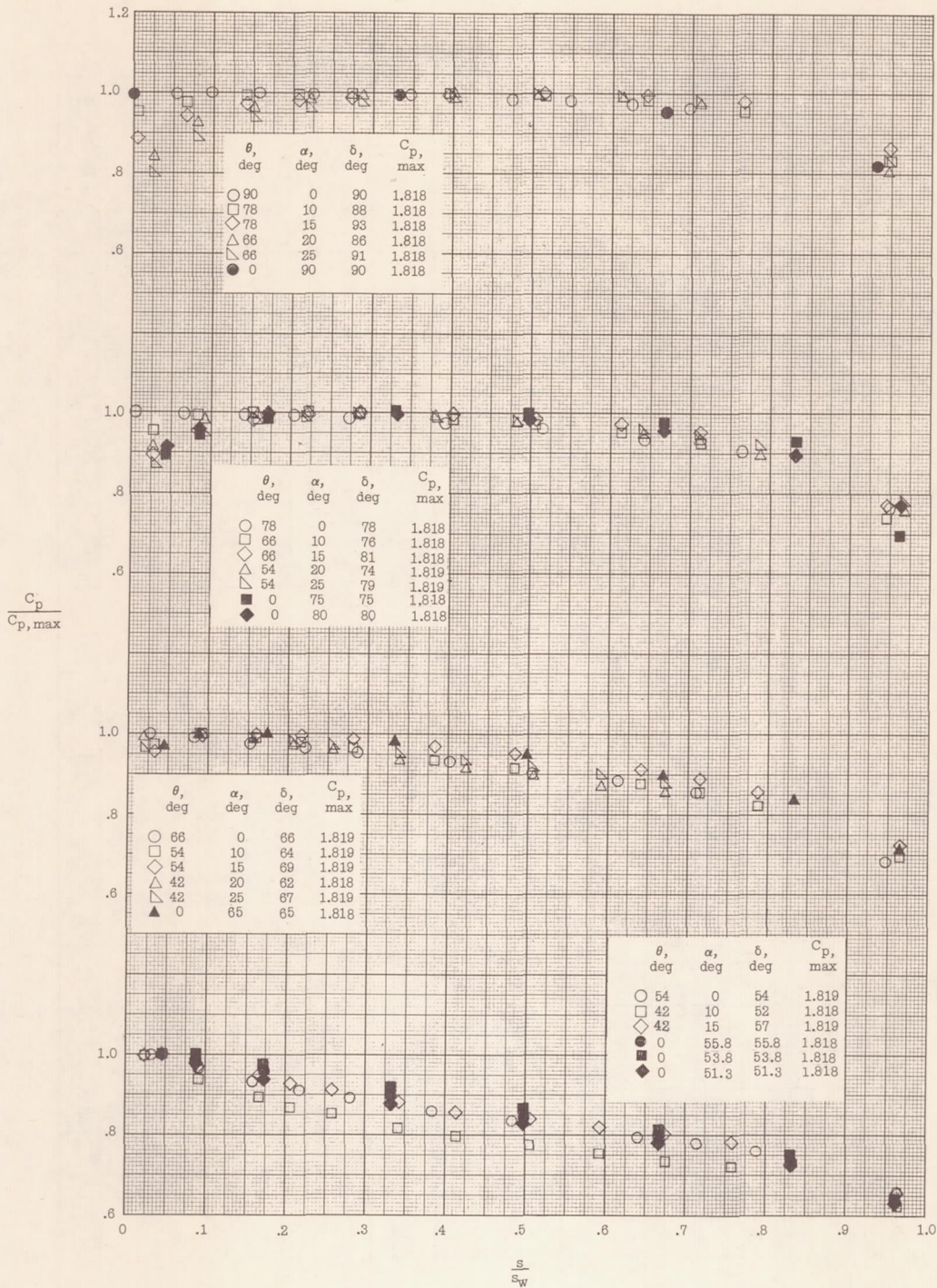
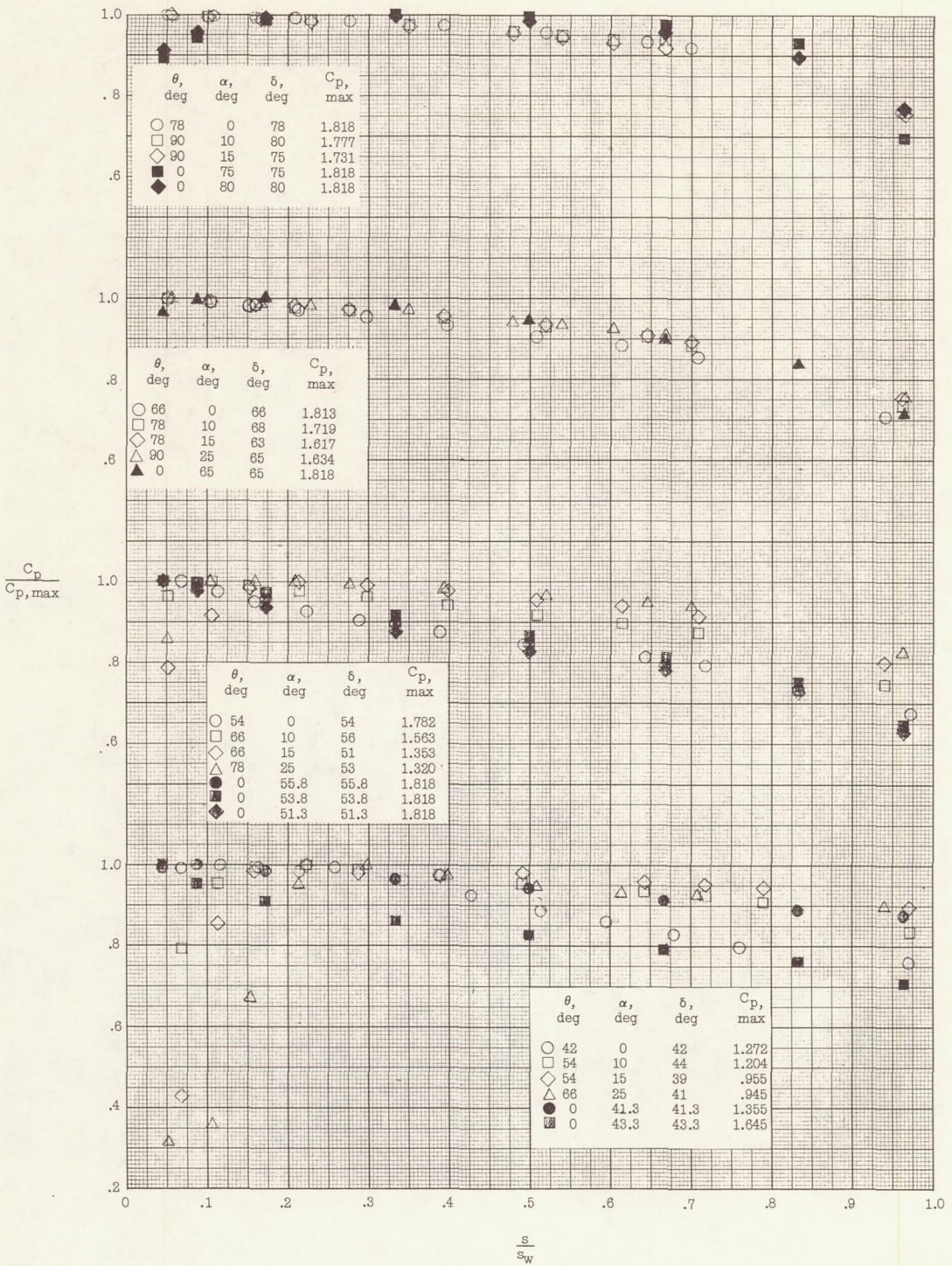
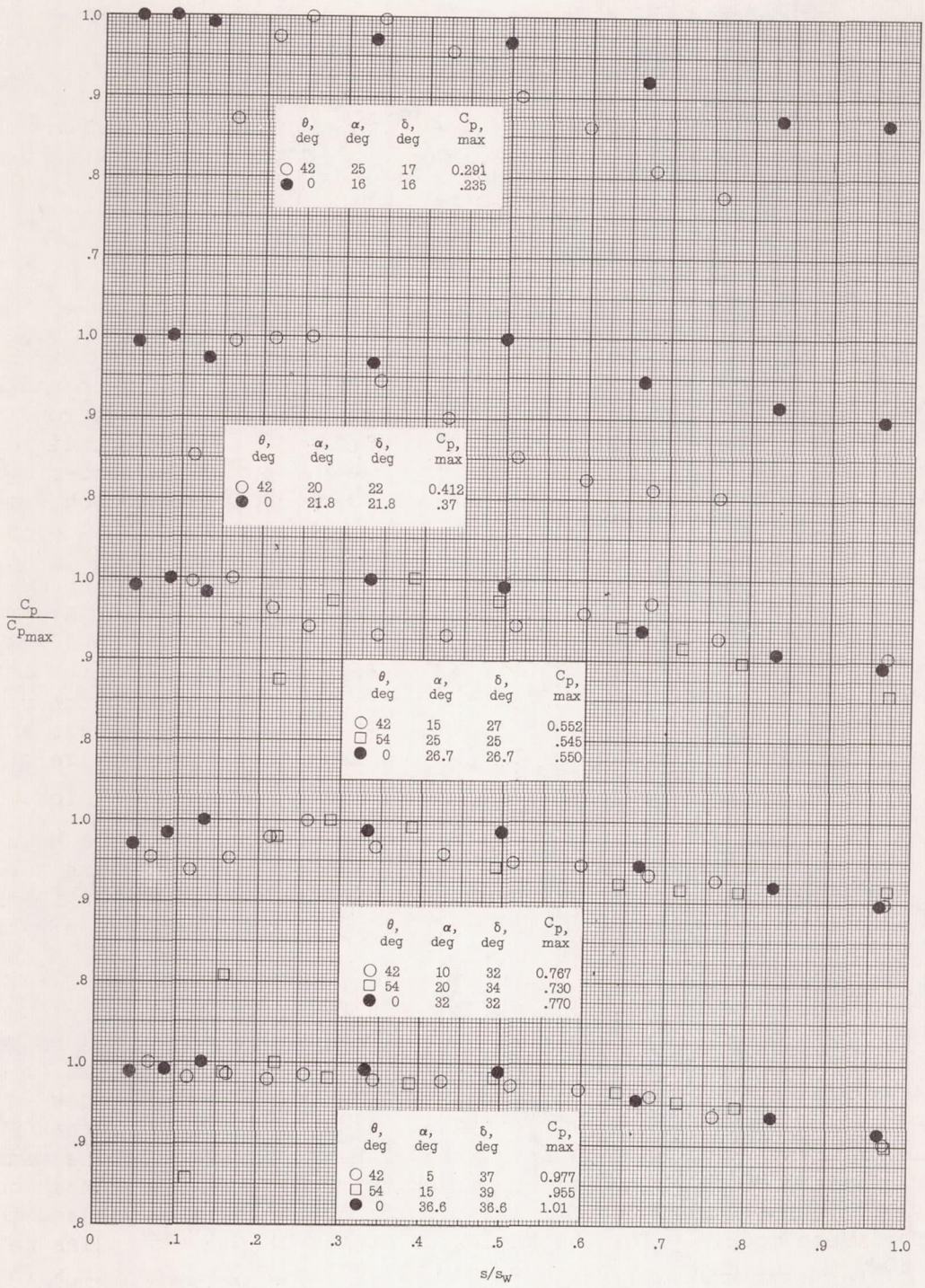


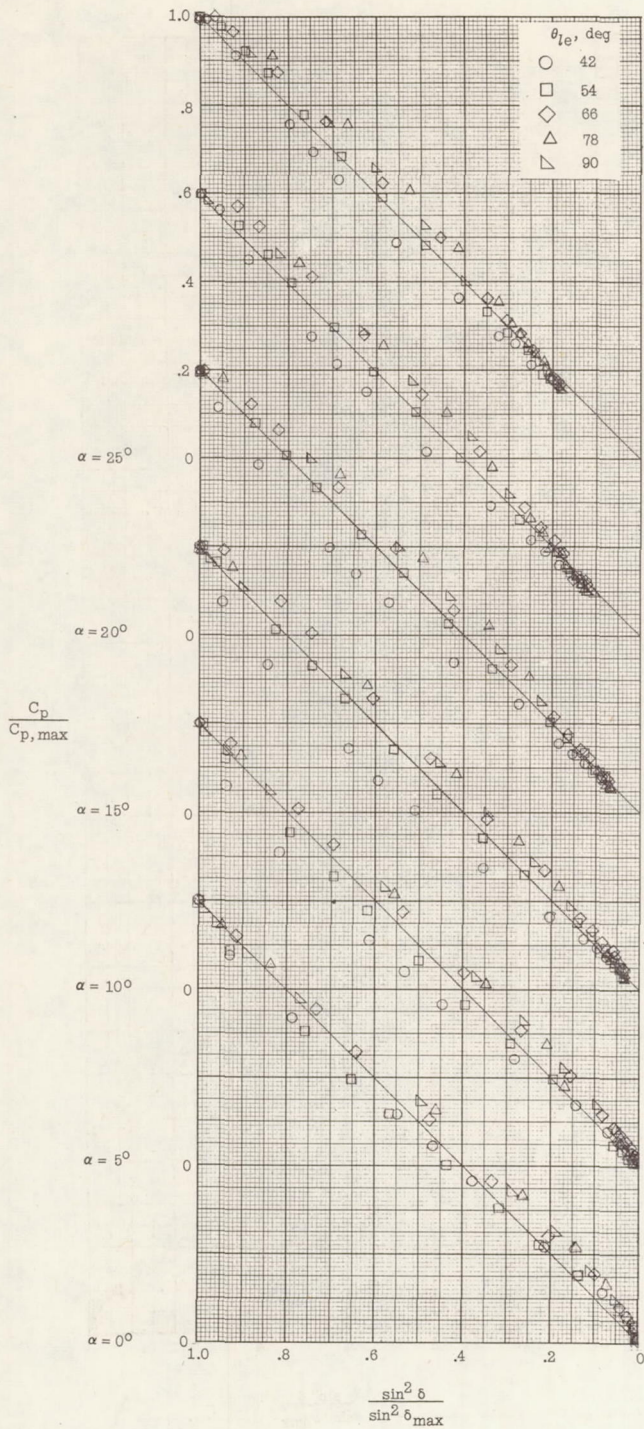
Figure 13.- Comparison of pressure distributions on wedges with constant deflection angles. Solid symbols are for flat-plate data at approximately the same deflection angles (ref. 2).



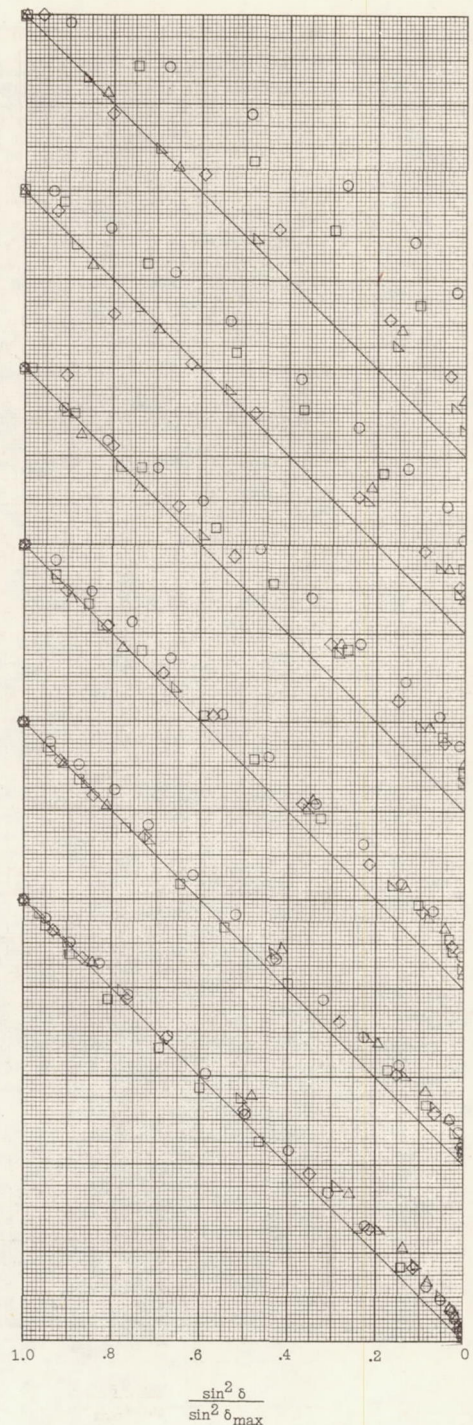


(b) Concluded.

Figure 13.- Concluded.

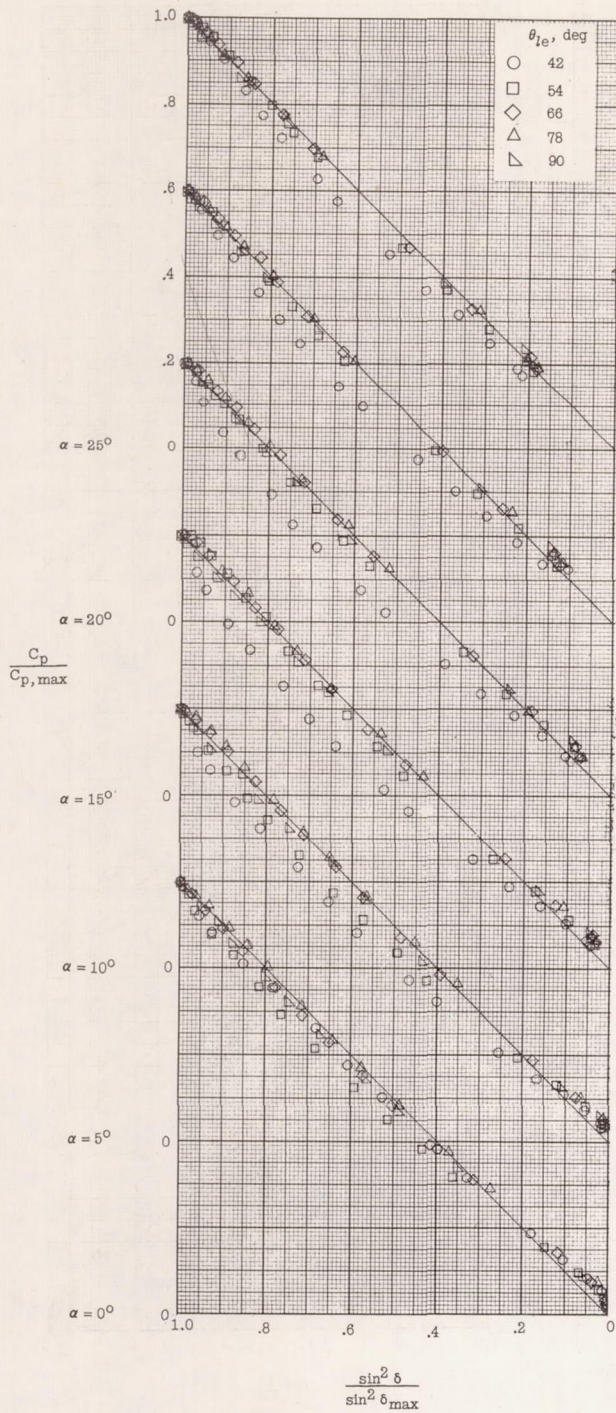


(a) Lower surface.

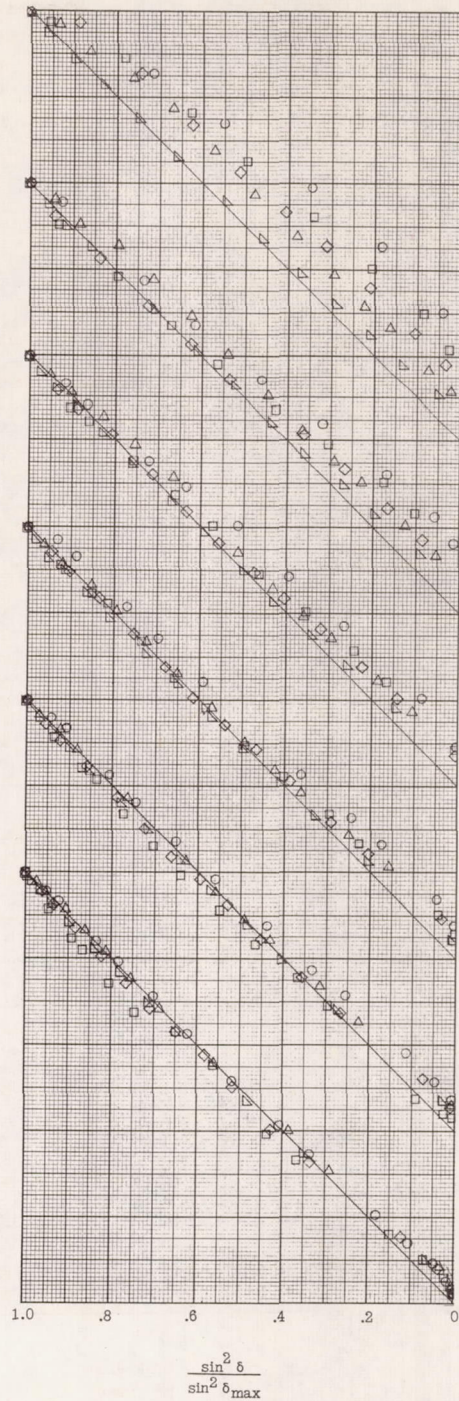


(b) Upper surface.

Figure 14.- Correlation of pressure distributions with generalized Newtonian theory for two-dimensional parabolic arc models.



(a) Lower surface.



(b) Upper surface.

Figure 15.- Correlation of pressure distributions with generalized Newtonian theory for two-dimensional circular arc models.